The Astrophysical Journal, 988:73 (15pp), 2025 July 20 https://doi.org/10.3847/1538-4357/adddb5

Efficient Ionizers with Low Hβ + [O III] Equivalent Widths: JADES Spectroscopy of a Peculiar High-redshift Population

Isaac H. Laseter[1], Michael V. Maseda[1], Charlotte Simmonds[2,3], Ryan Endsley[4], Daniel Stark[5], Andrew J. Bunker[6], Rachana Bhatawdekar[7], Kristan Boyett[6], Alex J. Cameron[6], Stefano Carniani[8], Mirko Curti[9], Zhiyuan Ji[5], Pierluigi Rinaldi[5], Aayush Saxena[6,10], Sandro Tacchella[2,3], Chris Willott[11], Joris Witstok[12,13], and Yongda Zhu[5]

[1] Department of Astronomy, University of Wisconsin-Madison, Madison, WI 53706, USA; Laseter@wisc.edu
[2] Kavli Institute for Cosmology, University of Cambridge, Madingley Road, Cambridge, CB3 0HA, UK
[3] Cavendish Laboratory, University of Cambridge, 19 JJ Thomson Avenue, Cambridge CB3 0HE, UK
[4] Department of Astronomy, University of Texas, Austin, TX 78712, USA
[5] Steward Observatory, University of Arizona, 933 North Cherry Avenue, Tucson, AZ 85721, USA
[6] Department of Physics, University of Oxford, Denys Wilkinson Building, Keble Road, Oxford OX1 3RH, UK
[7] European Space Agency (ESA), European Space Astronomy Centre (ESAC), Camino Bajo del Castillo s/n, 28692 Villanueva de la Cañada, Madrid, Spain
[8] Scuola Normale Superiore, Piazza dei Cavalieri 7, I-56126 Pisa, Italy
[9] European Southern Observatory, Karl-Schwarzschild-Strasse 2, 85748 Garching, Germany
[10] Department of Physics and Astronomy, University College London, Gower Street, London WC1E 6BT, UK
[11] NRC Herzberg, 5071 West Saanich Rd., Victoria, BC V9E 2E7, Canada
[12] Cosmic Dawn Center (DAWN), Copenhagen, Denmark
[13] Niels Bohr Institute, University of Copenhagen, Jagtvej 128, DK-2200 Copenhagen, Denmark

Received 2024 December 5; revised 2025 May 20; accepted 2025 May 26; published 2025 July 15

Abstract

Early JWST photometric studies discovered a population of UV-faint ($<L^*_{\rm UV}$) $z \sim 6.5$–8 Lyman break galaxies with spectral energy distributions implying young ages ($\sim$10 Myr) yet relatively weak Hβ + [O III] equivalent widths ($\rm EW_{H\beta + [O\,III]} \approx 400$ Å). These galaxies seemingly contradict the implicit understanding that young star-forming galaxies are ubiquitously strong Hβ + [O III] emitters, i.e., extreme emission line galaxies (EW $\gtrsim$750 Å). Low metallicities, high Lyman continuum escape fractions, and rapidly declining star formation histories have been proposed as primary drivers behind low Hβ + [O III] EWs, but the blend of Hβ + [O III] in photometric studies makes proving one of these scenarios difficult. We aim to characterize this peculiar population with deep spectroscopy from the JWST Advanced Deep Extragalactic Survey. We find that a significant subset of these galaxies at $z \gtrsim 2$ with modest Hβ + [O III] EWs ($\approx$300–600 Å) have high ionization efficiencies ($\log \xi_{\rm ion} \gtrsim 25.5$ Hz erg^{-1}). Suppressed [O III] EW values yet elevated Hα and Hβ EW values imply that the level of chemical enrichment is the primary culprit, supported by spectroscopic measurements of metallicities below $12 + \log({\rm O/H}) \approx 7.70$ ($0.1 Z_\odot$). We demonstrate that integrated Hβ + [O III] selections (e.g., Hβ + [O III] EW > 700 Å) exclude the most metal-poor efficient ionizers and favor (1) more chemically enriched systems with comparable extreme radiation fields and (2) older starbursting systems. In contrast, metallicity degeneracies are reduced in Hα space, enabling the identification of these metal-poor efficient ionizers by their specific star formation rate.

Unified Astronomy Thesaurus concepts: Emission line galaxies (459); High-redshift galaxies (734); Starburst galaxies (1570)

1. Introduction

The epoch of reionization, the last major phase transition of the Universe where intergalactic neutral hydrogen became ionized, likely results from UV emission produced from the formation of the first stars and galaxies in the Universe. Considering the pace of reionization (50% completion by $z \sim 7$–8; e.g., G. D. Becker et al. 2015; Planck Collaboration et al. 2020; S. E. I. Bosman et al. 2022), rapidly decreasing quasar luminosity functions above $z \gtrsim 3$ (e.g., P. F. Hopkins et al. 2007; C. J. Willott et al. 2010; X. Shen et al. 2020), and steep faint-end UV continuum luminosity functions ($\alpha \sim 2$) increasing toward higher z (e.g., R. J. Bouwens et al. 2015; S. L. Finkelstein et al. 2015; C. T. Donnan et al. 2023; L. Whitler et al. 2025), star-forming galaxies (SFGs) have advanced as the primary photon source for reionization. However, the degree to which these SFGs contribute to reionization, i.e., the physical mechanisms governing ionizing photon production and escape in the formation and evolution of galaxies, is extensively debated.

The effort in characterizing reionization-era SFGs began with establishing the presence of strong emission lines. Initial stellar population synthesis models applied to multiband $z \gtrsim 6$ photometry from the Hubble Space Telescope (HST) and Spitzer (e.g., L. P. Eyles et al. 2005, 2007; R. J. Bouwens et al. 2010; V. González et al. 2010; I. Labbé et al. 2010) suggested old (>100 Myr) and massive ($>10^9\ M_\odot$) stellar populations, immediately being at odds with galaxy model predictions of specific star formation rate (sSFR) evolution (e.g., K. Nagamine et al. 2010; R. Davé et al. 2011; S. M. Weinmann et al. 2011). The crucial caveat with these results was the exclusion of nebular emission and continuum in the population synthesis models. Strong nebular emission can photometrically masquerade as an old population considering the optical side of the Balmer break includes Hβ, [O III] $\lambda\lambda$4959, 5007, and Hα. Studies (e.g., D. Schaerer & S. de Barros 2009; Y. Ono et al. 2010; D. Schaerer & S. de Barros 2010; I. Labbé et al. 2013; R. Smit et al. 2014) demonstrated that incorporating nebular emission lowers SED-derived ages and raises sSFRs, though significant uncertainties in the inferred physical parameters remained considering the nebular contribution and photometric redshifts were derived from the same photometry. D. P. Stark et al. (2013) spectroscopically showed that accounting for nebular contributions decreases SED-derived masses by $\sim 2\times$, bringing sSFR measurements in line with theoretical predictions. However, D. P. Stark et al. (2013) could not access $z \gtrsim 5$ since Hα becomes unobservable from ground-based telescopes, and weaker lines were impractical to observe. JWST at this time was still approximately a decade away, but progress was still made at $z \lesssim 2$ where the rest-frame UV–optical was observable.

A. Van der Wel et al. (2011) identified an abundant population of $z \lesssim 2$ extreme emission line galaxies (EELGs) with comparable line strengths to those at higher redshift, but with the added detail that the emission originates from faint UV ($M_{\rm UV} > -20$) and low-mass ($\lesssim 10^{8.5}\ M_\odot$) galaxies comprised of young stellar populations (1–100 Myr). These results reflected evolutionary models (e.g., K. Nagamine et al. 2010; Z. Zheng et al. 2010; S. M. Weinmann et al. 2011) exploring intense and episodic star formation above $z \sim 3$, which was a key differentiating factor of this population relative to local blue compact dwarfs. For example, the sSFR of EELGs are an order of magnitude higher than local massive SFGs (e.g., M. V. Maseda et al. 2014). However, so-called "green peas," discovered in the Sloan Digital Sky Survey around the same time as high-z EELGs, exhibit comparable sSFRs and [O III] λ5007 EWs (up to $\sim$1000 Å; C. Cardamone et al. 2009; R. O. Amorín et al. 2010; A. E. Jaskot & M. S. Oey 2013; A. Henry et al. 2015). The interpretation of these local studies was that strong emission lines and extremely faint continua originate from low-mass systems undergoing an intense burst of star formation, analogous to $z \sim 2$ systems. The prevalence of bursty star formation was observed to increase strongly with redshift as gas depletion timescales substantially longer (several hundred million years) than the mass-weighted ages (50 Myr; e.g., M. V. Maseda et al. 2018) and nebular line ratios characteristic of high ionization parameters (e.g., N. A. Reddy et al. 2018b) were found. Equally important, M. Tang et al. (2019, hereafter T19) established EELGs as efficient ionizers using deep MMT and Keck spectroscopy at $z \sim 2$, finding higher Balmer and [O III] $\lambda\lambda$4959, 5007 EWs correspond to more efficient ionizing photon production. The overall interpretation emerged that high-z galaxies associated with intense Balmer and [O III] emission are important contributors to reionization.

However, JWST calls into question the ubiquity of the youngest galaxies possessing high Balmer and [O III] EWs. R. Endsley et al. (2023, hereafter E23), using the Cosmic Evolution Early Release Science Survey (CEERS) and `Beagle`, found a significant class of sub-L_* galaxies with young light-weighted ages ($\lesssim$50 Myr) yet relatively minor broadband excesses corresponding to weak Hβ + [O III] emission ($\lesssim$500 Å). More evolved systems with weak Hβ + [O III] λ5007 emission are most certainly expected, but a young, starbursting population exhibiting weak Hβ + [O III] emission would be comparatively rare relative to $z \lesssim 2$ results. E23 found the combination of young ages and relatively low Hβ + [O III] EWs ($\lesssim$600 Å) can be reproduced with low metallicities ($\sim 0.1 Z_\odot$). In such metal-poor models, [O III] emission is greatly weakened relative to the more "chemically evolved" galaxies near $\sim 0.2 Z_\odot$. Even though Balmer EWs increase with decreasing metallicity, the relative contribution of [O III] to Hβ + [O III] is generally far more dominant ([O III]/Hβ $\sim$ 5–10; C. C. Steidel et al. 2016; M. V. Maseda et al. 2018; R. L. Sanders et al. 2018; T19) such that extremely low metallicities result in Hβ + [O III] EWs atypical of $z \lesssim 2$ EELGs. E23 was a pure photometric study, so the role of metallicity in driving low Hβ + [O III] EWs in EELGs is ambiguous as high escape fractions of ionizing photons (<912 Å; $f_{\rm esc}$) into the intergalactic medium (IGM) and rapidly declining star formation histories (SFHs) were also proposed.

Equally important, however, it is not clear whether this population is comprised of efficient ionizers. The contribution of ionizing photons to reionization, i.e., the ionizing photon budget, includes the galaxy UV luminosity density ($\rho_{\rm UV}$), the ionizing photon escape fraction ($f_{\rm esc}$), and the ionizing photon production efficiency ($\xi_{\rm ion}$). $\xi_{\rm ion}$ represents the ionizing photon production rate per nonionizing UV luminosity ($L_{\rm UV}$) around 1500 Å:

$$\xi_{\rm ion}\ [\rm Hz\ erg^{-1}] = \frac{Q(H_0)}{L_{\rm UV}}, \tag{1}$$

with $Q(H_0)$ representing the intrinsic rate of ionizing photons in units of s^{-1}. $\xi_{\rm ion}$ measurements above $z \sim 2$ have gradually emerged over the last decade, with the primarily photometric results agreeing with the relations from T19 (e.g., D. P. Stark et al. 2015; K. Nakajima et al. 2016; D. P. Stark et al. 2017; D. Lam et al. 2019; M. V. Maseda et al. 2020). Interestingly, N. Emami et al. (2020), utilizing strong-lensed galaxy clusters (A1689, MACS J0717, and MACS J1149) with Keck/MOSFIRE spectroscopy, found $1 < z < 3$ low-mass galaxies exhibit higher $\xi_{\rm ion}$ at lower Hβ and [O III] λ5007 EWs compared to the relations from T19. In the era of JWST, $\xi_{\rm ion}$ has been found to be elevated and diverse ($\log \xi_{\rm ion} \gtrsim \approx 25.2 - 26.0$ Hz erg^{-1}; e.g., M. Castellano et al. 2023; G. Prieto-Lyon et al. 2023; C. Simmonds et al. 2023; H. Atek et al. 2024; R. Begley et al. 2025; S. Mascia et al. 2024; A. Saxena et al. 2024a; L. Shen et al. 2025; K. E. Heintz et al. 2025), suggesting an array of ionizing properties, ages, and metallicities, and aligning with the emergent picture from first 2 yr of JWST findings (e.g., A. J. Cameron et al. 2023b; K. Davis et al. 2024; H. Katz et al. 2023; J. E. Rhoads et al. 2023; J. R. Trump et al. 2023).

However, the significant population of young, sub-L_* galaxies identified in E23 with low Hβ + [O III] λ5007 EWs combined with the elevated ionization efficiencies now routinely measured above $z \sim 2$ suggests there is a population of metal-poor efficient ionizers that are abnormal to the [O III] trends associated with EELGs identified in T19. We aim to spectroscopically characterize the distribution of $\xi_{\rm ion}$ in the high-z Universe and attempt to explain the main driver behind low Hβ + [O III] EWs in young reionization-era galaxies using medium and deep spectroscopy from JADES.

The remainder of this paper is organized as follows. In Section 2 we briefly explain our JADES observations. In Section 3 we describe our flux and EW measurements and how we subdivide our JADES sample. In Section 4 we define the ionizing photon production efficiency and our methodology. In Section 5 we describe our incorporation of [O III] $\lambda4363$ emitters, $\hat{\rm R}$-derived metallicities, and photoionization modeling to further examine trends between nebular EWs and ionizing photon efficiencies. In Section 6 we discuss the role of metallicity driving low Hβ + [O III] EWs. Finally, in Section 7 we discuss the limitations of EELG selections employing [O III] in identifying extremely metal-poor SFGs. We include a short discussion on Case B departures in the Appendix. For this work, we adopt the Planck Collaboration et al. (2020) cosmology: $H_0 = 67.36$ km s^{-1} Mpc^{-1}, $\Omega_M = 0.3153$, and $\Omega_\Lambda = 0.6847$.

2. Observations

We summarize the JADES NIRSpec and NIRCam observations important for our work below, but we refer the reader to A. J. Bunker et al. (2023), D. J. Eisenstein et al. (2023), and F. D'Eugenio et al. (2025) for more general details. Briefly, the JADES program is a joint Guaranteed Time Observation (GTO) program between the NIRSpec and NIRCam Instrument Science Teams comprising two deep pointings and 14 medium-deep pointings in Great Observatories Origins Deep Survey South (GOODS-S) and GOODS North (GOODS-N; M. Giavalisco et al. 2004; proposal IDs 1180, 1181, 1210, 1286, and 3215). NIRSpec observations within each visit were performed as a three-shutter nod. The central pointing of each visit was dithered (by $<1''$) such that common targets were observed in different shutters and detector real estate. Thus, each visit had a unique MSA configuration, although the target allocation (performed with the eMPT)[14] was optimized for maximizing target commonality between all three dither positions. Priority classes were introduced to maximize NIRSpec's MSA with the highest priority targets (A. J. Bunker et al. 2023). These targets were observed in more than one pointing when possible, so some higher-priority targets have longer integration times. Regardless, the median exposure times across Deep/Medium observations and gratings totaled ∼90,000 s/∼6500 s (PRISM), ∼22,000 s/∼5400 s (G140M/F070LP), ∼15,000 s/∼5700 s (G235M/F170LP), and ∼19,400 s/∼5400 s (G395/F290LP). Total targets across all pointings number ∼4000 galaxies. For the reduction of NIRCam images, we refer the reader to M. J. Rieke et al. (2023; JADES Data Release 1 (DR1)), D. J. Eisenstein et al. (2023; JADES Data Release 2), and F. D'Eugenio et al. (2025; JADES Data Release 3). These recent photometry releases, used in the current work (Section 3.2), cover ∼56 arcmin^2 of NIRCam imaging in GOODS-N and GOODs-S, detecting ∼90,000 distinct objects. These data include seven overlapping pointings, each with 8–9 separate filters: F090W, F115W, F150W, F182M, F200W, F210M, F277W, F335M, F356W, and F410W. The median exposure time across all filters totaled ∼12,000 s. NIRSpec results are based on version 3 of the JADES reduction pipeline developed by the NIRSpec GTO team and the European Space Agency (P. Ferruit et al. 2022). Point-source path-loss corrections were considered by modeling each galaxy as a point-like source, considering its relative intrashutter position (F. D'Eugenio et al. 2025). Extended source path-loss corrections are currently being explored (M. Curti et al. 2025, in preparation).

3. Our Sample

3.1 Emission Line and Equivalent Width Measurements

We are concerned with how $\xi_{\rm ion}$ scales above $z \approx 2$ and the dominant mechanism(s) driving low Hβ + [O III] $\lambda5007$ EWs in young galaxies observed in E23. Our emission line complexes of interest are therefore [O II] $\lambda\lambda3727$, 3729, Hγ and [O III] $\lambda4363$, Hβ and [O III] $\lambda\lambda4959$, 5007, and Hα and [N II] $\lambda\lambda6548$, 6583. We measure fluxes by combining G140M/F070LP, G235M/F170LP, and G395M/F290LP grating/filters and simultaneously fitting Gaussian functions to each emission line complex with free parameters λ, FWHM, and the respective line amplitudes for 2496 JADES galaxies. We fit multiple Gaussians simultaneously to increase the fidelity of our fits to weaker emission features. We perform 1000 iterations of our fitting procedure using the observed error-weighted fluxes, taking the median and standard deviation of the fits as our respective fluxes and 68% confidence interval. If [O III] $\lambda4959$ or [O III] $\lambda5007$ were located within the detector gap we enforced an internal ratio of 1/2.98 of the measured value. We also apply a modest signal-to-noise ratio (S/N) cut of Hα and H$\beta \geqslant 5$ and [O III] $\lambda5007 \geqslant 5$ to preserve our initial JADES sample but ensure robust dust corrections and for no conversion from EW(Hα) to EW(Hβ) (i.e., no detector-gap conversion for Balmer lines; see the Appendix); this step narrows our initial sample to 307 galaxies.

It is difficult to apply a single active galactic nucleus (AGN) removal step for our population as $z \gtrsim 2$ Baldwin–Phillips–Terlevich demarcation lines are highly uncertain (L. J. Kewley et al. 2013; R. Maiolino et al. 2024; M. V. Maseda et al. 2023; R. L. Sanders et al. 2023a). We therefore visually inspect our line complexes for broadening and match our objects to Chandra observations imposing a $1''$ detection radius; we also crossmatch our sample with AGNs identified in JADES literature (e.g., J. Scholtz et al. 2025; J. Lyu et al. 2024). Our AGN removal procedure is not unequivocal as high-z AGNs are not necessarily detected with Chandra data (e.g., R. Maiolino et al. 2024; F. Pacucci & R. Narayan 2024) and broad line emission is viewing-angle dependent, in addition to the peculiar "little red dot" line widths measured (e.g., E. Lambrides et al. 2024). We emphasize that while $\xi_{\rm ion}$ is the ionizing photon efficiency from any ionizing source, our steps are necessary for a more pure SFG sample. We further restrict our sample by requiring a UV slope (β) bluer than -1.5 (described in Section 3.2) and EW$_{\rm H\alpha} > 100$ Å as this includes SFGs under a full range of nebular conditions (see H. Katz et al. 2024). These steps result in a total of 174 galaxies, for which we present the redshift distribution in Figure 1.

We now determine the Balmer and [O III] EWs for the current sample by first carefully inspecting the R100 spectra for clear continua detection. We define a 400 Å bin around the emission line complex of interest in the R100 spectrum, removing any emission within this window and taking the median as the continuum level. We then combine our R1000 fluxes and R100 continua to determine observed-frame EWs; we correct for R100 and R1000 flux differences as described in A. J. Bunker et al. (2023). Our EW fitting procedure is limited as we do not account for stellar absorption in our Balmer fits, though given the strength of the emission lines in our sample the effects of stellar absorption are insignificant (X. Kong et al. 2002; B. Groves et al. 2012). We compare our fitting techniques by employing the penalized pixel fitting (`ppxf`)

---

[14] https://github.com/esdc-esac-esa-int/eMPT_v1; N. Bonaventura et al. (2023).

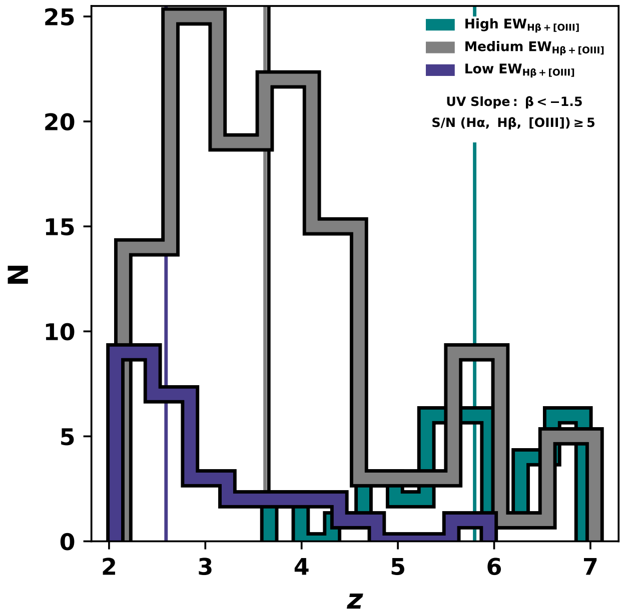

Figure 1. The redshift distribution of our high- ($\geqslant$750 Å), medium- (200–750 Å), and low-equivalent-width (EW) ($\leqslant$200 Å) Hβ+[O III] samples. We include the median redshift of our respective samples ($\bar{z}_{\rm High} = 5.80$, $\bar{z}_{\rm Medium} = 3.62$, and $\bar{z}_{\rm Low} = 2.59$) and complete sample (black line; $\bar{z}_{\rm Total} = 3.69$). The complexity of the the The James Webb Space Telescope (JWST) Advanced Deep Extragalactic Survey (JADES) selection function is prevalent, and thus we emphasize the current work is not intended as a magnitude-limited population study, but rather an investigation of seemingly atypical systems requiring deep spectroscopy, which JADES thoroughly provides. Our total sample numbers are 31, 116, and 27 for high-, medium-, and low-EW galaxies, respectively.

algorithm (M. Cappellari 2017, 2023). We omit a full description of the fitting techniques (see T. J. Looser et al. 2025); but briefly, ppxf models the continuum as a linear superposition of simple stellar population (SSP) spectra, using nonnegative weights and matching the spectral resolution of the observed spectrum. We use the high-resolution ($R = 10{,}000$) SSP library combining MIST isochrones (J. Choi et al. 2016) and the C3K theoretical atmospheres (C. Conroy et al. 2018) within ppxf. We fit for the same emission lines of interest as before using ppxf. We find little deviations in our derived fluxes and EWs between both methods (≈0.08% change). We therefore use the results of our emission line fitting procedure to remain as general as possible, i.e., not appointing a specific suite of SSP models for the analysis.

We correct for dust in our measurements from the available Balmer lines adopting a D. Calzetti et al. (2000) attenuation curve. We initially assume the theoretical ratios of $\rm H\alpha/H\beta = 2.86$, $\rm H\beta/H\gamma = 2.13$, and $\rm H\alpha/H\gamma = 6.11$ from Case B recombination at $T = 1.0 \times 10^4$ K. However, 29% (51/176) of our total sample possess Balmer ratios less than Case B, 17% (30/176) of which deviate by 1σ. These assumed intrinsic ratios are temperature dependent (D. E. Osterbrock & G. J. Ferland 2006), and nebular temperatures are routinely found to be greater than $T = 1.0 \times 10^4$ K (e.g., A. J. Taylor et al. 2022; I. H. Laseter et al. 2024; R. L. Sanders et al. 2023b; A. J. Cameron et al. 2024) resulting in a lower intrinsic ratio as the recombination coefficient is dependent on the n-level cross section and the temperature distribution of electrons. The temperature dependence is typically seen as minor, but the intrinsic ratio of $\rm H\alpha/H\beta$ becomes 2.78 even at $T = 1.5 \times 10^4$ K. We therefore relax our Case B assumption and allow $\rm H\alpha/H\beta = 2.78$ (corresponding to $T = 1.5 \times 10^4$ K); however, 26% (46/174) of our total sample still possess Balmer ratios lower than Case B in these conditions, 15% (26/176) of which deviate by 1σ. Our findings are not uncommon as Balmer emission lower than the Case B and A assumptions is frequent in the high-z Universe (e.g., L. Sandles et al. 2024; W. McClymont et al. 2025; H. Yanagisawa et al. 2024). We present a discussion of the effects of dust in the Appendix, but considering we do not have secure electron temperatures for the majority of our sample (Section 5.1), we decide to return to assuming Case B recombination at $T = 1.0 \times 10^4$ K. We do not correct for dust if our measured values are less than these theoretical values, but we identify non-dust-corrected galaxies in the corresponding figures. Ultimately, the self-comparative trends identified in this work are not affected by changing our dust law, but exact $\xi_{\rm ion}$[Hz erg^{-1}] values would likely change due to the respective handling of the UV. Even when employing non-Balmer dust corrections, such as infrared excess–β relations from N. A. Reddy et al. (2018a), our results remain.

3.2 UV Luminosities

We first determine the UV luminosities for our full JADES sample following the method outlined in T. Hashimoto et al. (2017). We define a spectral window of 200 Å around 1500 Å, mimicking the typical wavelength range used in SED codes (e.g., J. Chevallard & S. Charlot 2016). We therefore exclude Lyα emission and do not invoke any IGM modeling. We take the definition of UV continuum slopes as $f_\lambda \propto \lambda^\beta$, so the relation between AB magnitudes (J. B. Oke & J. E. Gunn 1983) and our spectral window is

$$m_{1500} = -2.5\log([1500\ \text{Å} \times (1+z)]^{\beta+2}) + A, \qquad (2)$$

where A is the spectral amplitude given in magnitude space. Our absolute magnitude ($M_{\rm UV}$) is therefore given by

$$M_{\rm UV} = m_{1500} - 5\log(d_L/10\ {\rm pc}) + 2.5\log(1+z), \qquad (3)$$

where $d_{\rm L}$ is the luminosity distance. We determine $M_{\rm UV}$ by applying a Monte Carlo technique for each object, perturbing our spectra by their respective observational errors and fitting the error-weighted spectral window 1000 times. We dust correct our $M_{\rm UV}$ values after converting the nebular color excess found through the Balmer decrement (Section 3.1) to stellar as described in D. Calzetti et al. (2000), i.e., $E(B-V)_{\rm stellar} = 0.44 * E(B-V)_{\rm gas}$. Finally, we determine $L_{\rm UV}$ by taking the median and standard deviation of the total runs as our respective values and 68% confidence interval. We routinely observe C IV $\lambda\lambda$1548, 1551 emission in our spectra, implying a metal-poor stellar population (e.g., M. W. Topping et al. 2024b). We verify these lines do not affect our $M_{\rm UV}$ measurements by masking C IV $\lambda\lambda$1548, 1551 and repeating our procedure, finding no change. The decision of our main UV spectral window limits our sample to $z \gtrsim 4$, but for the current study, viable info can be gathered down to $z \sim 2$, as well as connecting to the T19 relations. Therefore, we extend our UV range to 2300 Å for objects between $2 \leqslant z \leqslant 4$. We verify the current analysis remains unchanged with this additional step by refitting all $z \gtrsim 4$ galaxies under this criterion, finding no change. We confirm our spectra-derived UV luminosities are accurate by performing a similar analysis photometrically using NIRCam filters F070W, F090W, F115W, F150W, and F200W. We perform the same procedure

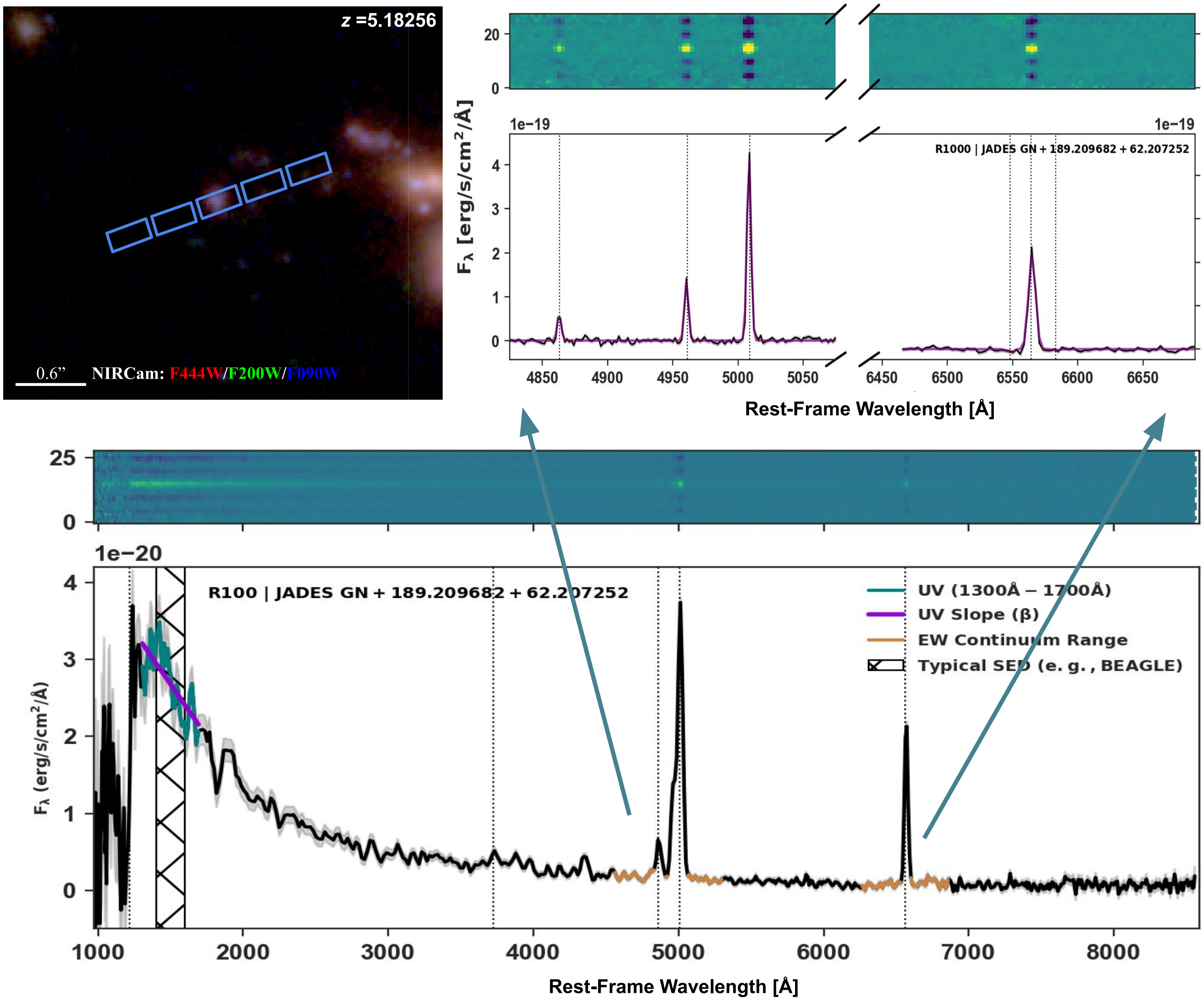

Figure 2. Top left: NIRCam F444W, F200W, and F090W (red–green–blue) image of JADES-GN+189.20968+62.20725 ($z = 5.18256$) with NIRSpec microshutter array (MSA) shutters overlaid. Bottom: R100 spectrum of JADES-GN+189.20968+62.20725. We identify our UV range as green and our derived β slope as purple. We shade a 100 Å bin centered at 1500 Å to demonstrate the common spectral energy density (SED)-derived UV slopes spectral range. Toward redder wavelengths, we identify the continuum range used in determining Balmer and [O III] EWs as orange (200 Å around the line center). The top panel shows a 2D spectrum with a clear continuum detection. The lines of interest (located at the vertical dotted lines) shown from left to right are Lyα, [O II] $\lambda\lambda$3727, 3729, Hβ and [O III] $\lambda\lambda$4959, 5007, and Hα. We show our measurement uncertainty as gray shaded regions. Top right: R1000 spectrum of JADES-GN+189.20968+62.20725. We emphasize our fits for Hβ and [O III] $\lambda\lambda$4959, 5007 and Hα, which are shown in purple. The top panels show the 2D spectrum for each respective line complex.

described above but with a spectral window of approximately 1300–2800 Å, similar to past works (e.g., E. R. Stanway et al. 2005; R. J. Bouwens et al. 2009; S. M. Wilkins et al. 2011; T. Hashimoto et al. 2017). The results of the current analysis remain unchanged when using NIRCam photometry, paralleling the findings of A. Saxena et al. (2024b) who compared NIRSpec-produced synthetic photometry with real NIRCam photometry (M. J. Rieke et al. 2023). We demonstrate our spectral UV slope fitting procedure in Figure 2 using object JADES-GN+189.20968+62.20725. We shade a 200 Å bin centered at 1500 Å to demonstrate the common SED-derived UV slopes spectral range; we also shade a 200 Å EW continuum window centered on the Hβ + [O III] and Hα complexes and include R1000 fits from Section 3.1.

3.3 The Final Samples

The inability to separate Hβ and [O III] creates difficulties in interpreting photometric results. With NIRSpec MSA spectroscopy we can separate these components to examine the respective nebular contributions and thus the underlying physical mechanisms, as well as the bias introduced when selecting on Hβ + [O III] EW in the high-z Universe (Section 7.1). We subdivide our sample into respective low, medium, and high-Hβ + [O III] EW samples; we choose the low Hβ + [O III] EW sample to be $\leqslant$200 Å, the medium Hβ + [O III] EW sample to be between 200 and 750 Å, and the high-Hβ + [O III] EW sample to be $\geqslant$750 Å, reflecting observations of high-z studies (e.g., K. Boyett et al. 2022; K. Davis et al. 2024; E23; K. Boyett et al. 2024). We

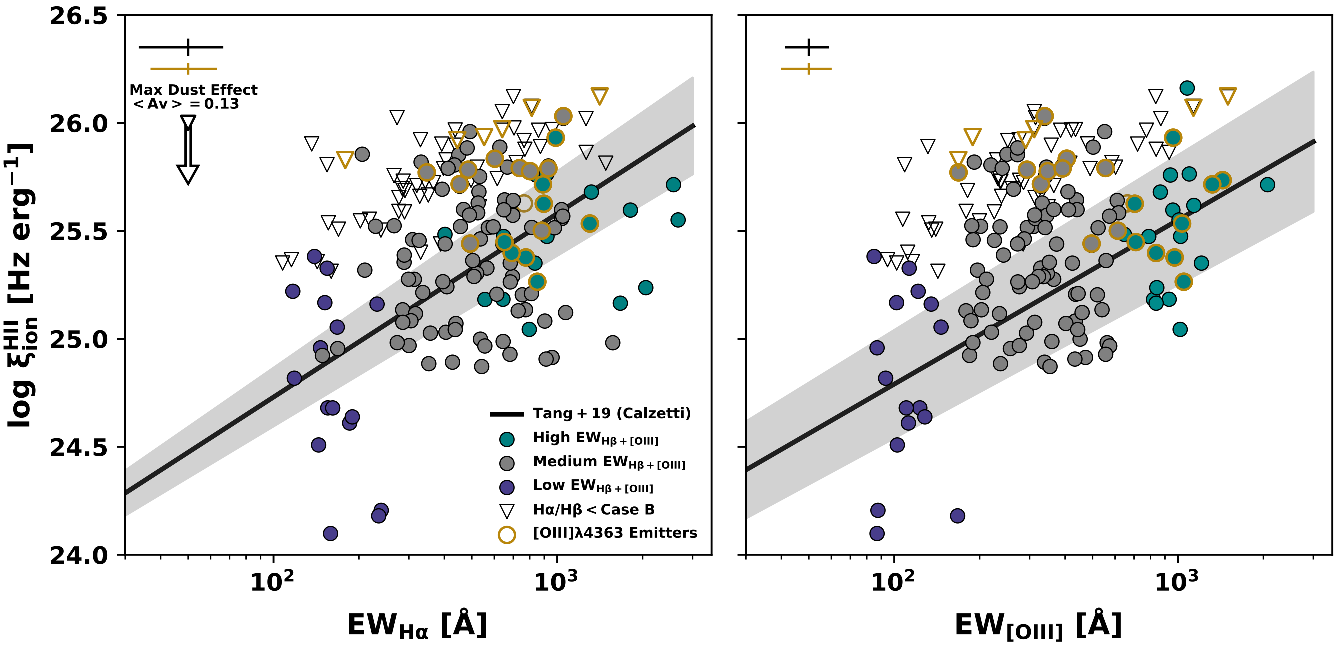

Figure 3. Left: correlation between $\log\xi_{\rm ion}^{\rm H\,II}$ and Hα EW for our high-, medium-, and low-EW samples. We include the HST-derived $z \sim 2$ relation with 68% confidence intervals from T19. We largely agree with the relation found from T19, but there is a clear overlap between our medium- and high-EW samples at higher Hα EWs. We identify our Case B departure systems as triangles and note the maximum dust effect taken from the average of our low-, medium-, and high-EW samples, though this effect is likely overestimated for this population (see the Appendix). We identify [O III] λ4363 emitters as gold outlines. Right: correlation between $\log\xi_{\rm ion}^{\rm H\,II}$ and [O III] λ5007 EW for our high-, medium-, and low-EW samples. [O III] dominance in Hβ + [O III] EWs is evident as there is little overlap in [O III] space. However, a significant population of our medium-EW sample has $\xi_{\rm ion}^{\rm H\,II}$ values similar to our high-EW sample, suggesting oxygen composition differences at comparable sSFRs. This systematic offset between Hα and [O III] is further evident in deviations from the HST-derived relation from T19 for [O III] EWs.

summarize our sample in Figure 1: 27 (15%) galaxies are within the low-EW bin, 116 (67%) within the medium-EW bin, and 31 (18%) within the high-EW bin. We stress, however, that JADES is not a magnitude-limited survey. As such, the current work is not intended as a full population analysis, but rather an investigation of seemingly atypical systems requiring deep spectroscopy, which JADES provides.

4. The Ionizing Photon Production Efficiency

Several variants of $\xi_{\rm ion}$ exist in the literature, so we explicitly define $\xi_{\rm ion}$ in Equation (1) as $\xi_{\rm ion}^{\rm H\,II}$ following the definition from J. Chevallard et al. (2018). $\xi_{\rm ion}^{\rm H\,II}$ includes the UV luminosity corrected for dust attenuation outside H II regions but not for dust attenuation inside H II regions nor for nebular continuum emission. SED-derived studies typically employ $\xi_{\rm ion}^{*}$, in which $L_{\rm UV}$ is the intrinsic stellar monochromatic UV luminosity ($\xi_{\rm ion}^{*}$), thus excluding dust and nebular emission/absorption. There is also simply $\xi_{\rm ion}$, which includes the observed (not dust corrected) $L_{\rm UV}$. The various definitions affect quoted results, so we compare against literature $\xi_{\rm ion}^{\rm H\,II}$ values unless otherwise noted.

$Q(H_0)$ in Equation (1) is not an observed quantity as there is photon escape from these regions, i.e., $Q_{\rm obs}(H_0) = (1 - f_{\rm esc})Q(H_0)$. $f_{\rm esc}$ is largely unconstrained (S. Mitra et al. 2013; J.-P. Paardekooper et al. 2015), resulting in some studies grouping $\xi_{\rm ion}^{\rm H\,II}$ and $f_{\rm esc}$ as a single parameter (e.g., K. Duncan & C. J. Conselice 2015). There is the added complexity of dust absorption of ionizing photons (e.g., S. Tacchella et al. 2022), which if accounted for increases $Q(H_0)$—the opposite effect of $f_{\rm esc}$. These competing effects are extraneous for our self-comparative work, so we set $f_{\rm esc} = 0$ and apply no correction for $Q(H_0)$ dust absorption. Regardless of what we set these values to, $Q_{\rm obs}(H_0)$ can be converted to an Hα luminosity[15] as in E. J. Murphy et al. (2011):

$$\xi_{\rm ion}^{\rm H\,II}\ [{\rm Hz\ erg^{-1}}] = 7.38 \times 10^{11}\left(\frac{L_{\rm H\alpha}}{L_{\rm UV}}\right). \tag{4}$$

We use Equation (4) to determine $\xi_{\rm ion}^{\rm H\,II}$ for our low-, medium-, and high-Hβ + [O III] λ5007 EW samples. We specifically report the median $\log\xi_{\rm ion}^{\rm H\,II}$ value for each galaxy after 1000 iterations of perturbing the measurement with our $L_{\rm H\alpha}$- and $L_{\rm UV}$-derived errors; our reported errors are taken as the standard deviation of the distribution of $\xi_{\rm ion}^{\rm H\,II}$ values. We find the median of our samples to be $\log\xi_{\rm ion}^{\rm H\,II} = 25.22$ Hz erg^{-1} (low), $\log\xi_{\rm ion}^{\rm H\,II} = 25.52$ Hz erg^{-1} (medium), and $\log\xi_{\rm ion}^{\rm H\,II} = 25.52$ Hz erg^{-1} (high) with corresponding standard deviations of 0.48, 0.33, and 0.27 dex, similar to the $z \gtrsim 2$ results of M. Castellano et al. (2023), G. Prieto-Lyon et al. (2023), C. Simmonds et al. (2023), H. Atek et al. (2024), R. Begley et al. (2025), S. Mascia et al. (2024), A. Saxena et al. (2024a), L. Shen et al. (2025), and K. E. Heintz et al. (2025). We present in Figure 3 our Hα EWs and [O III] λ5007 EWs with $\xi_{\rm ion}^{\rm H\,II}$, respectively, and compare against HST-derived $z \sim 2$ relations from T19.

Interestingly, we observe a systematic offset between EW$_{\rm H\alpha}$ and EW$_{\rm [O\,III]}$ at fixed $\xi_{\rm ion}^{\rm H\,II}$ between our medium- and high-EW samples. Specifically, above $\log\xi_{\rm ion}^{\rm H\,II} \geqslant 25.5$ Hz erg^{-1} our medium-EW sample exhibits Hα EWs comparable to our high-EW sample ($\gtrsim$600 Å) while simultaneously exhibiting

---

[15] Temperature and density will also affect the conversion from $Q(H_0)$ to Hα, though at the typical temperatures we measure in Section 5.1, these differences are below the systematic trends with metallicity that we identify in this work.

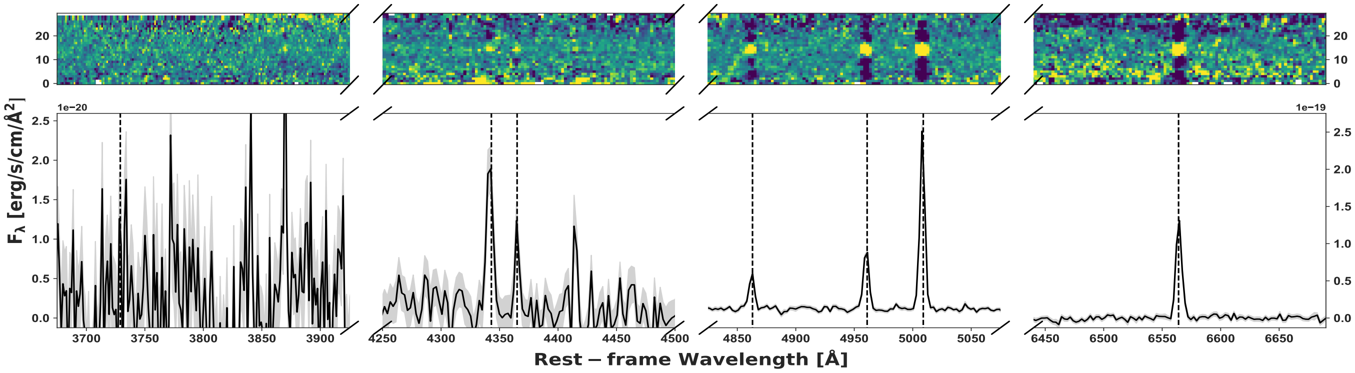

Figure 4. JWST/NIRSpec R1000 spectrum for our newly reported [O III] λ4363 emitter JADES-GN+189.16215+62.26381 with a metallicity of $12 + \log(\mathrm{O/H}) = 7.30 \pm 0.12$ at $z = 6.3$. The lines of interest (located at the vertical dotted lines) shown from left to right are [O II] $\lambda\lambda$3727, 3729, Hγ, [O III] λ4363, Hβ, [O III] $\lambda\lambda$4959, 5007, and Hα. [O II] $\lambda\lambda$3727, 3729, Hγ, and [O III] λ4363 (Hβ, [O III] $\lambda\lambda$4959, 5007, and Hα) share the same y-axis. The top panels show the 2D spectrum for each respective line complex. We show our measurement uncertainty as gray shaded regions.

low [O III] EWs (∼300 Å). We perform a Welch's t-test (unequal variances t-test; B. L. Welch 1947) between our medium- and high-EW samples for galaxies with $\log \xi_{\mathrm{ion}}^{\mathrm{H\,II}} \geqslant 25.5$ Hz erg^{-1}. For EW$_{\mathrm{H}\alpha}$, we find a t-statistic of 1.17 with a p-value of 0.25, indicating that our medium- and high-EW distributions overlap and the separation between their respective means is not statistically significant. In comparison, for EW$_{\mathrm{[O\,III]}}$, we find a t-statistic of 12.22 with a p-value of 9.51×10^{-14}, indicating our sample distributions do not overlap and the separation between their respective means is statistically significant. This distinction in nebular EW and $\xi_{\mathrm{ion}}^{\mathrm{H\,II}}$ space is not seen in the $z \lesssim 2$ T19 sample, indicating a physically motivated difference above $z \gtrsim 2$. Interestingly, Y. Zhu et al. (2025), using the Systematic Mid-infrared Instrument Legacy Extragalactic Survey (SMILES) program, found the relation between $\xi_{\mathrm{ion}}^{\mathrm{H\,II}}$ and EW$_{\mathrm{[O\,III]}}$ to be shallower relative to T19 while the Hα relation still agrees, similar to our findings. The selection functions of SMILES (S. Alberts et al. 2024) and JADES (A. J. Bunker et al. 2023; D. J. Eisenstein et al. 2023; F. D'Eugenio et al. 2025) differ, so it is promising that there are corroborating results, though the underlying causes still have not been explored. Further, P. Rinaldi et al. (2023, 2024), using medium and broadband NIRCam/MIRI imaging, demonstrated diverse [O III] λ5007/Hβ ratios ($-1 \lesssim \log(\mathrm{[O\,III]}\ \lambda5007/\mathrm{H}\beta) \lesssim 1.5$) at high H$\alpha$ EWs and $\log \xi_{\mathrm{ion}}^{\mathrm{H\,II}}$ values ($\gtrsim$25.5 Hz erg^{-1}), suggesting the Hβ + [O III] photometric flux excess is not necessarily always driven by [O III] $\lambda\lambda$4959, 5007 and that elevated $\log \xi_{\mathrm{ion}}^{\mathrm{H\,II}}$ values are still expected at lower [O III] EWs. As mentioned, E23 proposed extremely low metallicities, high f_{esc}, and rapidly declining star formation rates (SFRs) as possible solutions to their young, low Hβ + [O III]λ5007 EW sample.

It is difficult for us to comment on f_{esc} as we cannot measure it directly, but as $\xi_{\mathrm{ion}}^{\mathrm{H\,II}}$ is defined by $Q(H_0)$, we do not expect a decrease in [O III] EW at fixed $\xi_{\mathrm{ion}}^{\mathrm{H\,II}}$ if f_{esc} was high. Likewise, the relative decrease in [O III] EW between the high- and medium-EW samples at fixed $\xi_{\mathrm{ion}}^{\mathrm{H\,II}}$ is apparent for $\log \xi_{\mathrm{ion}}^{\mathrm{H\,II}} \gtrsim 25.5$ Hz erg^{-1}, requiring the presence of recently formed O-type stars (M. V. Maseda et al. 2020; H. Katz et al. 2024, see Section 7.1), therefore indicative of recent or ongoing star formation rather than a decline. Moreover, as we present in the next section, the electron temperatures of galaxies aligning with these trends range between 10,000 and 25,000 K, indicative of recent star formation. Extremely low metallicities remain the most likely candidate driving low Hβ + [O III] EWs seen in the current work. We now focus on examining the role of metallicity in $\xi_{\mathrm{ion}}^{\mathrm{H\,II}}$ and nebular EWs.

5. Metallicity Derivations and Photoionization Modeling

I. H. Laseter et al. (2024) and R. L. Sanders et al. (2023b) demonstrated a clear failure of locally derived strong-line calibrations in the high-z Universe due to elevated excitation ratios at fixed metallicity, especially at metallicities lower than $0.1Z_{\odot}$ ($12 + \log(\mathrm{O/H}) \approx 7.7$). R. L. Sanders et al. (2023b) provided high-z calibrations using early CEERS observations, whereas I. H. Laseter et al. (2024) proposed the so-called $\hat{\mathrm{R}}$ calibration involving a different projection in the space defined by log([O II] $\lambda\lambda$3727, 3729/Hβ) (R2), log([O III] λ5007/Hβ) (R3), and metallicity. We continue with approximating metallicities using the $\hat{\mathrm{R}}$ calibration from I. H. Laseter et al. (2024) and the R3 calibration from R. L. Sanders et al. (2023b) depending on the S/N of [O II] $\lambda\lambda$3727, 3729 as described in Section 6. Our following conclusions are unaffected by interchanging these calibrations, but galaxy-by-galaxy cases do differ. We, therefore, use the diagnostic power of JWST to further identify a large sample of [O III] λ4363 emitters to more robustly investigate metallicity in nebular EW and $\xi_{\mathrm{ion}}^{\mathrm{H\,II}}$ space.

5.1. [O III] λ4363 Emitters

I. H. Laseter et al. (2024) identified 10 [O III] λ4363 emitters in JADES DEEP-HST (A. J. Bunker et al. 2024) in the GOODS-S legacy field; we have now increased this number to 60 with our additional JADES observations (Section 2). We follow our analysis as described in Sections 3 and 4 for this specific sample while deriving electron temperatures and metallicities as described in I. H. Laseter et al. (2024). Our final [O III] λ4363 sample for the current work is 31 as we impose a [O III] λ4363 S/N > 3 restriction (the median S/N in our [O III] λ4363 sample is ∼4.25), exclude [O III] λ4363 emitters lacking UV coverage, and remove those with broad Balmer emission and electron temperatures above $T_{\mathrm{e}} \geqslant 30{,}000$, since these are beyond the physical range associated with the earliest O-type star (e.g., O3, $T_{\mathrm{eff}} \approx 40{,}000$ K; P. Massey et al. 2004). The latter sample is intriguing, based on predictions of hotter stars and nebular continuum contribution (A. J. Cameron et al. 2024; H. Katz et al. 2024), but these galaxies require more careful electron temperature derivations that we leave for forthcoming work. We present in Figure 4 the [O II] $\lambda\lambda$3727, 3729, Hγ and [O III] λ4363, and Hβ and [O III] $\lambda\lambda$4959, 5007 complexes for JADES-GN+189.16215+62.26381, a $z = 6.3$ novel [O III] λ4363 emitter with $12 + \log(\mathrm{O/H}) = 7.30 \pm 0.12$ and $\log \xi_{\mathrm{ion}}^{\mathrm{H\,II}} = 25.8 \pm 0.01$ Hz erg^{-1}.

In Figure 3 we include our [O III] λ4363 emitters. Qualitatively, it is clear our [O III] λ4363 sample is representative of the JADES medium- and high-EW samples in nebular EW and $\xi_{\mathrm{ion}}^{\mathrm{H\,II}}$ parameter space, including the leftward systematic offset from the T19 [O III] EW relation apparent in our medium-EW sample. Similar to our statistical separation between our medium- and high-EW samples in [O III] space, when we compare the statistical separation of our [O III] λ4363 sample to our high-EW sample, we find a t-statistic of 3.43 with a p-value of 0.001, indicating a statistically significant separation. In contrast, in Hα space, we find a t-statistic of 0.01 with a p-value of 0.99, indicating no significant separation. We measure t_3 values between ≈13,000 and 23,000 K, which are nebular temperatures associated with the presence of OB-type stars and recent star formation, aligning with the notion that the leftward systematic offset at fixed $\xi_{\mathrm{ion}}^{\mathrm{H\,II}}$ with EW$_{\mathrm{[O\,III]}}$ is not from the reduction or loss of ionizing photons. We now incorporate our [O III] λ4363 sample and strong-line-derived metallicities with spectral synthesis and photoionization models to further explore the disparities between Balmer and [O III] EWs with $\xi_{\mathrm{ion}}^{\mathrm{H\,II}}$.

5.2. BPASS + CLOUDY

The entirety of our derived values depend on the recombination or collisional excitation within H II regions, and thus the nature of the young stellar populations creating these regions. We therefore utilize `BPASS v2.2.1` (J. J. Eldridge & E. R. Stanway 2009) spectral synthesis predictions as our spectral model inputs for our current study. `BPASS` does not explicitly include nebular emission, so we utilize available `CLOUDY`-processed (G. J. Ferland et al. 2017) `BPASS` models [16] (L. Xiao et al. 2018). In general, these models assume $n_e = 200\,\mathrm{cm}^{-3}$ while varying $\log(U)$ between -1.0 and -4.0 with dust grains included, using the favored model from the `BPASS` collaboration (`v2.2.1 imf135_300`) including a broken upper initial mass function (IMF) slope of -1.35, an upper mass limit of 300 $M_{\odot}$, and an instantaneous burst; the covering fraction was set to 1.0, thus matching our assumption of $f_{\mathrm{esc}} = 0$ (Section 4). Modeling nebular gas conditions with `CLOUDY` involves an array of free parameters, and thus results can vary widely when comparing individual H II regions to assumed models. We stress that we are not modeling the individual galaxies in our sample, but rather examining global properties driving the systematic offset in Figure 3, and thus these `BPASS + CLOUDY` models suffice for our purposes. We include $\log(U)$ models of -1.0, -2.0, and -3.0 ranging between ∼2 and ∼10 Myr after the star formation event. We note for this exercise that we report the model ionization efficiency defined as $\xi_{\mathrm{ion}}^{\star}$ in Section 4, as we are concerned with the intrinsic stellar populations (see Section 7.1 for a discussion of the relation with $\xi_{\mathrm{ion}}^{\mathrm{H\,II}}$). We now examine the effects of age, ionization, and metallicity in EW and $\xi_{\mathrm{ion}}^{\mathrm{H\,II}}$ space.

6. The Role of Ionization Parameter, Metallicity and Age

We first investigate if variations in the ionization parameter (U) could lead to the systematic offset we observe. We fix our `BPASS + CLOUDY` models at ≈2 Myr post-star-forming event, finding our models predict an increased [O III] λ5007 EW leftward offset at fixed $\xi_{\mathrm{ion}}^{\mathrm{H\,II}}$ when large variations in $\log(U)$ are present ($-1 \gtrsim \log(U) \gtrsim -3$). However, we observe the `BPASS + CLOUDY` models reproduce our Hα EW distribution and scatter when $\log(U)$ is between ≈-1.5 and -2, as expected. In general, to account for the full [O III] λ5007 EW offset, $\log(U)$ values $\gtrsim -1$ would be required, well beyond the reported values of SFGs in the high-z Universe (e.g., N. A. Reddy et al. 2023) and what is typically predicted (G. A. Blanc et al. 2015). We therefore investigate the offset induced with age and metallicity by fixing our `BPASS + CLOUDY` models to $\log(U) = -2.0$, varying ages between ≈2 and 10 Myr, and tracking `BPASS` metallicities in our parameter spaces. We see in the left panel of Figure 5 that the observed relation between Hα EW and $\xi_{\mathrm{ion}}^{\mathrm{H\,II}}$ is largely set by the age of the star formation event, with metallicity accounting for less scatter compared to $\log(U)$. In the right panel of Figure 5, the observed scatter between [O III] λ5007 EW and $\xi_{\mathrm{ion}}^{\mathrm{H\,II}}$ cannot be fully explained by starburst age, but the relation itself likewise is. In fact, at fixed metallicity, increasing the time since the star-forming event traces the relation from T19, while simultaneously, the `BPASS + CLOUDY` models demonstrate an ∼0.7 dex difference in [O III] λ5007 EWs between $6.5 \lesssim 12 + \log(\mathrm{O/H}) \lesssim 7.7$. In other words, extremely low-metallicity models indicate the largest directional offset between [O III] λ5007 EW and $\xi_{\mathrm{ion}}^{\mathrm{H\,II}}$ relative to the $z \sim 2$ relations.

It is advantageous to then focus on the medium-EW sample overlap in Hα EW space. We therefore select all galaxies from our medium-EW sample with Hα EW $\geqslant 400$ Å and $\log \xi_{\mathrm{ion}}^{\mathrm{H\,II}} \geqslant 25.5$ Hz erg^{-1}. We present in the lower panel of Figure 5 our [O III] λ4363 sample and medium-EW subsample overlaid on the `BPASS + CLOUDY` models from the upper panel. We color code these galaxies by metallicity, indicating $\sim 0.1 Z_{\odot}$ as the turnover color. We require a 2σ [O II] $\lambda\lambda$3727, 3729 detection to derive metallicities using $\hat{\mathrm{R}}$, else we employ the R3 calibration from R. L. Sanders et al. (2023b; instead of reporting metallicity upper limits). Both $\hat{\mathrm{R}}$ and R3 are double branched, and we do not significantly detect [N II] λ6584 or [S II] $\lambda\lambda$6717, 6731 in this population to break the degeneracies. Instead, we use our [O II] $\lambda\lambda$3727, 3729 measurements and 2σ upper limits derived directly from the noise spectrum following A. J. Cameron et al. (2023b) as the degeneracy breaker for the calibrations.

As predicted from the `BPASS + CLOUDY` models, we observe a general offset between the derived metallicities with increasing $\xi_{\mathrm{ion}}^{\mathrm{H\,II}}$ and decreasing EW$_{\mathrm{[O\,III]}}$ that is not necessarily observed at fixed EW$_{\mathrm{H}\alpha}$. Seventy-one percent (22/31) of our [O III] λ4363 population is less than $\sim 0.1 Z_{\odot}$ (median $12 + \log(\mathrm{O/H}) = 7.54$), coinciding with the greater dynamic range of our `BPASS + CLOUDY` models; likewise, there is the tendency of more metal-poor galaxies in our medium-EW subsample to possess lower EW$_{\mathrm{[O\,III]}}$, aligning with the nonlinear metallicity effects on EW$_{\mathrm{[O\,III]}}$.

We do observe a few enriched systems ($12 + \log(\mathrm{O/H}) \gtrsim 8.0$) above $z \sim 2$ relations at moderate [O III] EWs (∼400–600 Å), however. These metallicities are near where our models predict EW$_{\mathrm{[O\,III]}}$ peaks at fixed $\xi_{\mathrm{ion}}^{\mathrm{H\,II}}$, but I. H. Laseter et al. (2024) and R. L. Sanders et al. (2023b)

---

[16] Details of these `CLOUDY` models can be found here: https://bpass.auckland.ac.nz/4.html.

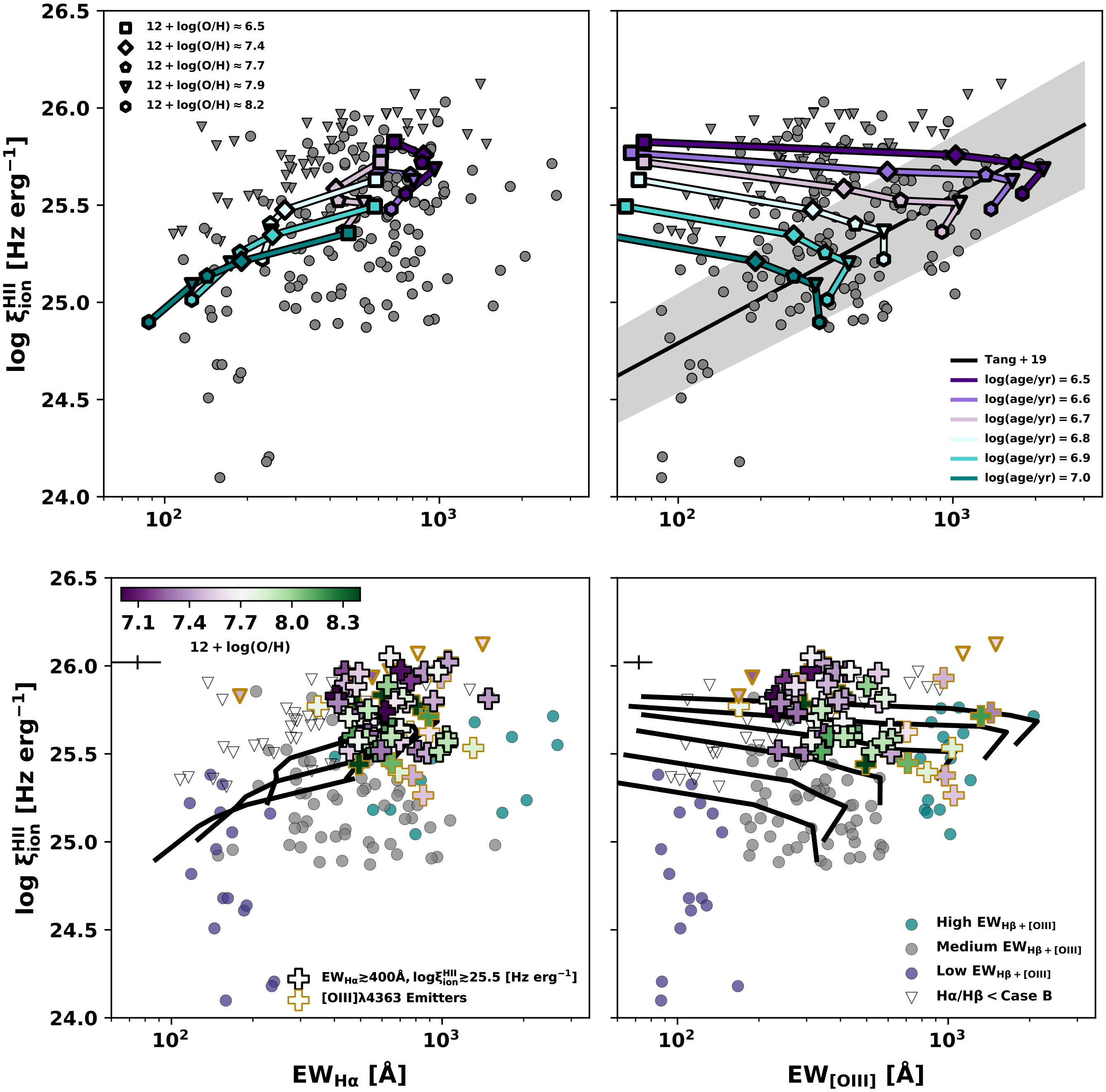

Figure 5. Top left: change in age of starburst at fixed $\log(U) = -2$ with `BPASS + CLOUDY` models including dust in Hα EW space; we indicate the respective model metallicity changes as well. As assumed, metallicity is minor compared to the effect of $\log(U)$ between Hα EW and $\xi_{\rm ion}^{\rm H\,II}$. Top right: the same `BPASS + CLOUDY` models but in [O III] EW space. We see that `BPASS + CLOUDY` predict a nonlinear leftward offset at fixed $\xi_{\rm ion}^{\rm H\,II}$ when the metallicities are lower than $12 + \log({\rm O/H}) \lesssim 7.70$ ($0.1Z_\odot$), similar to our observed leftward offset (∼1 dex) in our medium-EW sample, exhibiting comparable $\log\xi_{\rm ion}^{\rm H\,II}$ values (Figure 3). Between model metallicities of $7.70 \lesssim 12 + \log({\rm O/H}) \lesssim 8.20$ (i.e., the dynamic range in which the [O III]'s sensitivity to metallicity variations is reduced), increasing the time from the star formation event reproduces the derived relation from T19 (shaded region). Bottom left: same as above but medium-EW galaxies with $\log\xi_{\rm ion}^{\rm H\,II} \geqslant 25.5$ Hz erg^{-1} and [O III] λ4363 emitters are color coded by metallicity (Section 5). The `BPASS + CLOUDY` models predict a diminishing metallicity effect at high Hα EWs, aligning with the observed scatter in metallicity measurements. Bottom right: the efficient ionizers from the medium-EW sample and [O III] λ4363 emitters in [O III] space. A metallicity gradient is observed to lower [O III] EWs and higher $\log\xi_{\rm ion}^{\rm H\,II}$ values, aligning with the predicted trends of the `BPASS + CLOUDY` models. This gradient occurs since galaxies with metallicities less than $12 + \log({\rm O/H}) \lesssim 7.70$ ($0.1Z_\odot$) are disproportionately offset to lower [O III] EWs relative to more enriched counterparts with similar ionization efficiencies.

demonstrated elevated excitation ratios at these metallicities in the high-z Universe. It is therefore expected for more chemically evolved systems to scatter upward in the presence of harder ionization fronts and starbursting episodes, especially as $\xi_{\rm ion}^{\rm H\,II}$ is directly dependent on ionizing photon production. Extremely metal-poor AGNs are still an option even though we have not detected any broad or high ionization lines as an AGN presence would result in erroneous $T_{\rm e}$ values based on our current derivations (O. L. Dors 2021). Regardless, these outliers underscore the overlay between extremely low metallicities and starbursting episodes in more evolved systems.

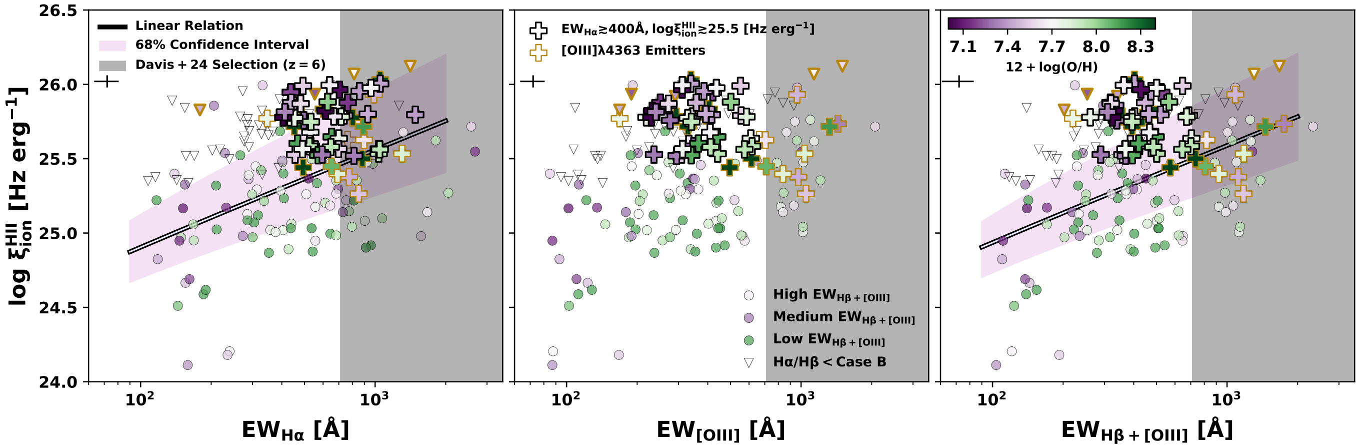

Figure 6. Correlation between $\xi_{\rm ion}^{\rm H\,II}$ and Hα EW (left), [O III] EW (center), and Hβ + [O III] EW (right) with data color coded to their $T_{\rm e}$-derived or $\hat{\rm R}$-derived metallicities. Equation (5) and our Hβ + [O III]-derived linear relation (see Section 7.2) are overlaid with 68% confidence intervals. The gray shaded region represents the selection function of D23 at $z = 6$. It is apparent EW$_{\rm H\alpha}$ is a more direct selection of extremely metal-poor ionizers compared to a selection involving [O III]. The Hβ + [O III] EELG selection function of D23, which is reasonable based on prior [O III]–$\xi_{\rm ion}^{\rm H\,II}$ scaling relations, disproportionately excludes these galaxies compared to a selection on Hα alone. This effect is also seen in our derived relations considering we underestimate $\xi_{\rm ion}^{\rm H\,II}$ for the extremely metal-poor population when using Hβ + [O III] yet align with the Hα relation found in T19 that better predicts $\xi_{\rm ion}^{\rm H\,II}$ within our confidence region. The physical limitations of $\xi_{\rm ion}^{\rm H\,II}$ combined with EWs > 1000−1500 Å in both Hα and Hβ + [O III] requiring more careful treatment (e.g., dominant nebular contributions, H. Katz et al. 2024; and AGNs, D23) is likely decreasing the apparent metallicity trends at EW$_{\rm H\beta}$ + [O III] $\gtrsim$ 1000 in our sample. Within the general high-z EW distribution though, a sole selection of Hβ + [O III] EW will bias to more chemically evolved starbursting systems at fixed $\xi_{\rm ion}^{\rm H\,II}$.

In fact, our extremely metal-poor galaxies deviate from the notion that the most intense (and efficient) radiation fields are exclusively found at the most extreme [O III] EWs ($\gtrsim$600 Å). It is not that extreme [O III] EWs lack young stellar populations, but that the effect of metallicity cannot be ignored when selecting with [O III] in the high-z Universe. The high Hα EWs we measure for our extremely metal-poor galaxies reflect sSFRs associated with the lowest-mass and youngest galaxies experiencing starbursting episodes above the star-forming main sequence, aligning with our measured ionization efficiencies. However, low metallicities have the effect of increasing the Hα EW, so our interpretations are ambiguous so far, requiring further discussion of $\xi_{\rm ion}^{\rm H\,II}$.

7. Discussion

7.1. Nature and Selection of Extremely Metal-poor Efficient Ionizers

We have spectroscopically demonstrated extremely metal-poor efficient ionizers are common above $z \gtrsim 2$, and that the dissimilar trends between Balmer and [O III] EWs with $\xi_{\rm ion}^{\rm H\,II}$ in the high-z Universe are caused primarily by oxygen abundances lower than 12 + log(O/H) ≈ 7.7 (0.1$Z_\odot$). These galaxies are comparatively rare in pre-JWST $z \sim 2$ and $z \sim 7$ samples as it is above 12 + log (O/H) ≈ 7.7 where oxygen has a weak dependence on metallicity yet high [O III]/Hβ ratios (e.g., R3 and R23; R. Maiolino & F. Mannucci 2019), especially as the dynamic range of [O III]'s sensitivity is reduced in the high-z Universe (I. H. Laseter et al. 2024; R. L. Sanders et al. 2023b). Metallicity effects were therefore diminished and the luminosity-weighted ages setting the Balmer and [O III] EW relations with $\xi_{\rm ion}^{\rm H\,II}$ were more apparent, though T19 did predict redshift evolution in [O III].

Specifically, $\xi_{\rm ion}^{\rm H\,II}$ does not have a strong dependence on metallicity relative to EW([O III]) (H. Katz et al. 2024), resulting in a flattening within this parameter space at low metallicities. In a compounding effect, decreasing metallicity disproportionately drives the [O III] EW below or near the typical selection limits of EELGs, thus limiting the identification of extremely metal-poor ionizers. For example, K. Davis et al. (2024, D23), selected 1165 EELGs in CEERS by imposing an observed-frame EW ⩾ 5000 Å cutoff in Hβ + [O III] λ5007 and Hα (i.e., rest-frame EW > 1000, 714 Å for $z = 4$, 6). D23 found their sample density was high near this detection limit, suggesting a continuous distribution to lower EWs. We present in Figure 6 the [O III], Hα, and Hβ + [O III] EW distributions with $\xi_{\rm ion}^{\rm H\,II}$ color coded by metallicity, including the D23 selection limit at $z = 6$.

We observe a continuous distribution to lower Hα and Hβ + [O III] EWs, but with the key detail that high $\xi_{\rm ion}^{\rm H\,II}$ values are maintained down to EW$_{\rm H\beta}$ + [O III] ≈ 300–400 Å. Regarding our medium-EW subsample, 98% (51/52) of these galaxies overlap with the Hα EW distribution of our high-EW sample, while 0% overlap with the Hβ + [O III] distribution. Therefore, in addition to a continuous distribution to lower Hβ + [O III] EWs at fixed $\xi_{\rm ion}^{\rm H\,II}$, we find that the H$\beta$ + [O III] EW is not a one-to-one selection with Hα.

The effectiveness of Hα EW selecting extremely metal-poor ionizers reflects the underlying trends of Hα EW with sSFR (e.g., E. Mármol-Queraltó et al. 2016). However, high Hα EWs do not exclusively mean higher sSFRs considering the effect of line blanketing driving Hα emission at low metallicities (S. Dreizler & K. Werner 1993; G. Gräfener et al. 2002). For example, R. Endsley et al. (2024) followed up E23 with NIRCam imaging from JADES (DR1), finding dissimilar Hβ + [O III] distributions between their faint ($M_{\rm UV} \approx -17.5$) and bright ($M_{\rm UV} \approx -20$) samples yet nearly identical Hα distributions, similar to our findings. R. Endsley et al. (2024) derived an ∼1 dex decrease in metallicity (`Beagle` derived) between their bright and faint samples, with the peak of the faint distribution being at 12 + log(O/H) = 7.40 (∼0.05$Z_\odot$) and the bright at 12 + log(O/H) = 8.06 (∼0.25$Z_\odot$). Such a decrease in metallicity results in a 50% increase in Hα EW according to R. Endsley et al. (2024) using the J. Gutkin et al. (2016) models. As such, R. Endsley et al. (2024) proposed low metallicities in

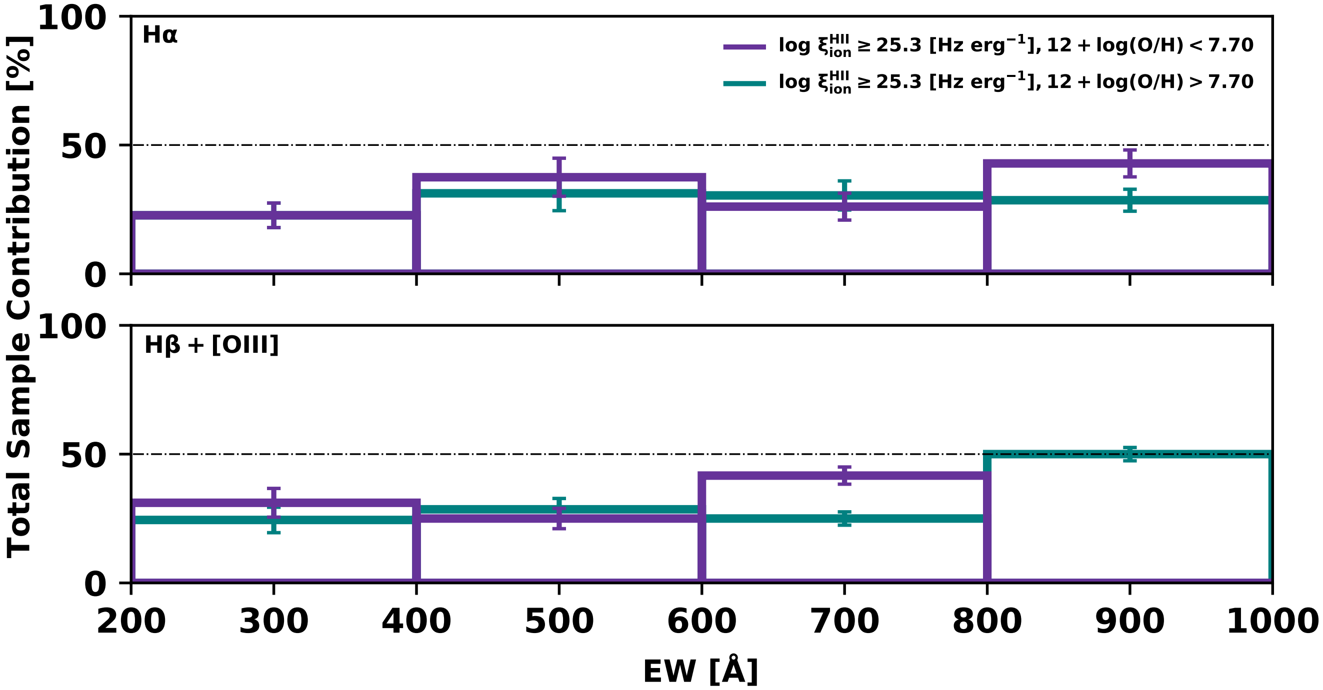

Figure 7. Top: $EW_{H\alpha}$ and the contributing percentage of extremely metal-poor (12 + log(O/H < 7.7); purple) and enriched (12 + log(O/H > 7.7); green) efficient ionizers (log $\xi_{ion}^{H\,II} \gtrsim 25.3$ Hz erg^{-1}). Metallicity subsamples contribute comparable amounts to the Hα EW and $\xi_{ion}^{H\,II}$ distributions, reflecting the dominant dependency of Hα EW and $\xi_{ion}^{H\,II}$ on ionizing photon production compared to metallicity. Bottom: the contributing fraction of efficient ionizers with respect to $EW_{H\beta + [O\,III]}$. The contributing percentages of our respective metallicity samples deviate with $EW_{H\beta + [O\,III]}$, largely an effect from extremely metal-poor galaxies offsetting disproportionately left from more chemically enriched systems with similar $\xi_{ion}^{H\,II}$ values.

the faint population, but the addition of a relative downturn in star formation did not increase the Hα EW relative to their UV bright population, reflecting bursty star formation. Considering our medium-EW sample extends down to $M_{UV} \approx -17$ while having weakened Hβ + [O III] EWs along the `BPASS + CLOUDY` model age traces in Hα (Figure 5), chemically poor galaxies in a relative downturn in star formation are naturally in our sample.

However, our `BPASS + CLOUDY` models suggest a diminishing effect of metallicity in driving Hα EWs with decreasing starburst age, such that at more extreme starbursts there is not a drastic Hα EW increase. The median Hα EWs of our high-EW and medium-EW subsamples are 896 and 628 Å, respectively, well within the range where metallicity effects are reduced. Moreover, it is below $12 + \log(O/H) \approx 7.0$ ($0.02Z_\odot$) where the largest increase of Hα occurs, but given the nebular metallicity "floor" (C. Kobayashi & A. Ferrara 2024) and our derived metallicities, it is unlikely that we have a large sample of sub-$12 + \log(O/H) = 7.0$ galaxies inflating Hα EWs to the extremes we measure. We also measure log $\xi_{ion}^{H\,II}$ values greater than 25.5 Hz erg^{-1} down to $EW_{[O\,III]} \approx 300$ Å. Recalling the specific definitions of ionization efficiency outlined in Section 4, H. Katz et al. (2024) demonstrated across various SSP models that the observed ionization efficiency ($\xi_{ion}^{H\,II}$) and the ionization efficiency associated with the intrinsic stellar population (ξ_{ion}^{*}) agree below log $\xi_{ion}^{H\,II} = 25.5$ Hz erg^{-1}, whereas above $\xi_{ion}^{H\,II}$ deviates low compared to ξ_{ion}^{*}. Therefore, our high $\xi_{ion}^{H\,II}$ values are expected to be associated with even higher intrinsic ionization efficiencies from young stellar populations. H. Katz et al. (2024) considered ages up to 20 Myr assuming an instantaneous burst, though at these extremely low metallicities, the inferred SFHs are likely younger. For example, the majority of the bright population from R. Endsley et al. (2024) is distributed between log $\xi_{ion}^{H\,II} \approx 25.5 - 25.6$ Hz erg^{-1} with an average positive SFR_{3Myr}/SFR_{50Myr} (∼1.5). This log $\xi_{ion}^{H\,II}$ median is comparable to the median of our medium-EW subsample (log $\xi_{ion}^{H\,II} = 25.7$ Hz erg^{-1}), but in contrast, the average metallicity of their bright population is $12 + \log(O/H) \approx 8.0$–8.1 ($0.2$–$0.25Z_\odot$) compared to $12 + \log(O/H) \approx 7.5$–7.6 ($0.07$–$0.08Z_\odot$) for our specific population, suggesting more pristine interstellar medium conditions. We argue then that in addition to the findings of the more general population studies of E23 and R. Endsley et al. (2024), there exist extremely metal-poor ionizers exhibiting large Hα EWs (≳600 Å) that are indeed starbursting galaxies rather than "artificially" boosted metal-poor galaxies in a relative starbursting lull. We note that our emission line selection (Section 3.3) preferentially allows us to find these low-metallicity galaxies as opposed to systems with star formation downturns, as found in E23 and R. Endsley et al. (2024).

Regardless of how one quantifies burstiness, we demonstrate that customary Hβ + [O III] EW selections (e.g., EW(Hβ + [O III]) > 700 Å) favor more chemically evolved SFGs around $7.8 \lesssim 12 + \log(O/H) \lesssim 8.3$ ($\gtrsim 0.2Z_\odot$) compared to a selection on Balmer EW alone. We present in Figure 7 the fraction of extremely metal-poor ($12 + \log(O/H) < 7.7$) and enriched ($12 + \log(O/H) > 7.7$) efficient ionizers (log $\xi_{ion}^{H\,II} \geqslant 25.3$ Hz erg^{-1}) relative to our total sample in 200 Å EW bins. We choose log $\xi_{ion}^{H\,II} \geqslant 25.3$ Hz erg^{-1} as this exceeds the so-called "canonical value" (log $\xi_{ion}^{H\,II} = 25.2 - 25.3$ Hz erg^{-1}; B. E. Robertson et al. 2013). As expected, metallicity subsamples contribute comparable amounts to the Hα EW and $\xi_{ion}^{H\,II}$ distributions, reflecting the dominant dependency of Hα EW and $\xi_{ion}^{H\,II}$ on ionizing photon production compared to metallicity. The near constant 50% contribution of efficient ionizers reflects the intrinsic scatter of our sample being nearly symmetric around the relation from T19. More interestingly, there are dissimilar trends in the contribution of extremely metal-poor and enriched systems dependent upon $\mathrm{EW}_{\mathrm{H}\beta+[\mathrm{O\,III}]}$. This effect is largely from the observed metallicity gradient in Figure 6 where extremely metal-poor galaxies exhibit Hβ + [O III] EW distributions of values similar to more evolved systems that have begun to lose their most massive stars, resulting in a separation with $\xi_{\mathrm{ion}}^{\mathrm{H\,II}}$. These extremely metal-poor galaxies then reside in $\mathrm{EW}_{\mathrm{H}\beta+[\mathrm{O\,III}]}$ distributions of more evolved systems that have begun to lose their most massive stars, resulting in a separation with $\xi_{\mathrm{ion}}^{\mathrm{H\,II}}$. The effect is then at typical EW distributions of the high-z Universe (e.g., K. Boyett et al. 2024; K. E. Heintz et al. 2025; G. Roberts-Borsani et al. 2024), as sole selection on Hβ + [O III] EW will bias to more (1) chemically enriched systems experiencing similar ionizing fronts and (2) evolved starbursting systems.

However, the $\mathrm{EW}_{\mathrm{H}\beta+[\mathrm{O\,III}]}$ metallicity gradient observed in our medium-EW subsample is not necessarily apparent in our high-EW sample, and the contribution of extremely metal-poor efficient ionizers begins to increase above $\mathrm{EW}_{\mathrm{H}\beta+[\mathrm{O\,III}]} \approx 1000$ Å. This is primarily due to the limited sample above $\mathrm{EW}_{\mathrm{H}\beta+[\mathrm{O\,III}]} \approx 1000$ Å (e.g., K. Boyett et al. 2024), but in general, such high EWs are near the extremes of models with younger stellar populations (e.g., S. M. Wilkins et al. 2020). Rest-frame Hβ + [O III] EWs from 1000−5000 Å have been measured with JWST, but they are a small percentage of the EELG distribution (K. Boyett et al. 2024). Additionally, the contributions of AGN and nebular continuum are beginning to be explored in these populations, for example, some higher EWs correspond to more compact emission regions (D23) and the EW distribution of nebular-dominated galaxies exceeds the general population of EELGs (H. Katz et al. 2024). Additionally, the physical limit of $\xi_{\mathrm{ion}}^{\mathrm{H\,II}}$ has the effect of flattening the observed EW–$\xi_{\mathrm{ion}}^{\mathrm{H\,II}}$ trend and creating a plateau at extremely high EWs. As such, we do not expect our observed trends to necessarily hold past $\mathrm{EW}_{\mathrm{H}\beta+[\mathrm{O\,III}]} \sim 1500$ Å as metallicity effects are diminished compared to possible nonstellar ionizing sources and extreme nebular temperatures and densities (H. Katz et al. 2024). Regardless, extremely metal-poor SFGs within more typical high-z EW distributions have nonnegligible metallicity effects when measuring $\mathrm{EW}_{\mathrm{H}\beta+[\mathrm{O\,III}]}$.

Because [O III]-deficient, ionizing systems are comparatively missed under normal Hβ + [O III] selections, it is uncertain whether Hβ + [O III]-selected EELGs are representative of the entire population of extremely metal-poor efficient ionizers. Systems with high sSFRs at the lowest metallicities are key in characterizing high-z IMFs and SFHs; key frameworks that have already been invoked in more significant manners in the high-z Universe, e.g., more top-heavy (K. Inayoshi et al. 2022; A. J. Cameron et al. 2024; S. Chon et al. 2024; E. R. Cueto et al. 2024; Z. Guo et al. 2024; L. Y. A. Yung et al. 2024; F. Cullen et al. 2025; A. Hutter et al. 2025) and bursts (A. Pallottini & A. Ferrara 2023; G. Sun et al. 2023a, 2023b; M. W. Topping et al. 2024a). These systems are also interesting for investigating the onset and evolution of the mass–metallicity relation and fundamental metallicity relation (e.g., M. Curti et al. 2023a, 2024; K. E. Heintz et al. 2023; K. Nakajima et al. 2023; A. Sarkar et al. 2025; D. Scholte et al. 2025) given the pristine gas likely in these galaxies. A deeper examination of the relative abundance ratios for our most metal-poor efficient ionizers is of interest as well considering the various proposed enrichment scenarios of peculiar abundance ratios found at high z (e.g., A. J. Cameron et al. 2023a; C. Kobayashi & A. Ferrara 2024). Fortunately, the most metal-poor SFGs can be identified by the ratio of Hα to Hβ + [O III] photometrically. Still, a deeper examination at fainter magnitudes is required considering that C. Simmonds et al. (2024) find a minor increase in $\xi_{\mathrm{ion}}^{\mathrm{H\,II}}$ for fainter galaxies with burstier SFHs in JEMS and JADES NIRCam imaging. Additionally, R. Endsley et al. (2024) found two-component and continuous SFHs differ drastically in `Beagle` epoch of reionization predictions, with continuous models systemically increasing f_{esc} to fainter M_{UV} SFHs and two-component models assuming small f_{esc} regardless of M_{UV}, thus forcing a downturn in star formation within their faint populations. N. Choustikov et al. (2024) demonstrated, however, that a single parameter cannot predict f_{esc} without large scatter, such that f_{esc} requires several observable quantities (eight in their model). In this context and that of C. Simmonds et al. (2024)'s findings, exploring highly efficient ionizers in extremely metal-poor environments with the theoretical bases of N. Choustikov et al. (2024) and H. Katz et al. (2024) could better characterize the role of the faint end of the UV luminosity function in reionization. Likewise, the escape of ionizing photons is not instantaneous with their production (N. Choustikov et al. 2024; A. Saxena et al. 2024a). It is of interest then to examine the emergence of escape channels in the most extremely metal-poor efficient ionizers, i.e., how $\xi_{\mathrm{ion}}^{\mathrm{H\,II}}$ values corrected for f_{esc} scale with more general properties (e.g., surface SFR and gas density) in the presence of young stellar populations.

7.2. The Use of Nebular Equivalent Widths as a Proxy for $\xi_{\mathrm{ion}}^{\mathrm{H\,II}}$

The discussion from the preceding section indicates EW(Hα) is a strong indicator of $\xi_{\mathrm{ion}}^{\mathrm{H\,II}}$. We therefore provide an updated relation between EW(Hα) and $\xi_{\mathrm{ion}}^{\mathrm{H\,II}}$ by fitting an error-weighted linear function for 10,000 iterations:

$$\log \xi_{\mathrm{ion}}^{\mathrm{H\,II}}\,[\mathrm{Hz\,erg^{-1}}] = (0.63 \pm 0.14) \times \log(\mathrm{EW}_{\mathrm{H}\alpha}\,[\text{Å}]) + (23.64 \pm 0.35). \quad (5)$$

We present our derived relation with 1σ (68%) confidence regions in the left panel of Figure 6. The slope of Equation (5) is 37% shallower than T19 and has a 2.7% higher intercept. These differences likely reflect the methodology in calculating L_{UV}. In particular, T19 inferred L_{UV} from their best-fitting `Beagle` models using a 100 Å bin centered at 1500 Å, and thus assumed a photoionization model and set of parameters. In comparison, we do not employ stellar population synthesis models in our continuum fitting and we extend our UV range to longer wavelengths (Section 3.2), thus small $\xi_{\mathrm{ion}}^{\mathrm{H\,II}}$ differences at fixed Hα EW are expected. However, Equation (5) introduces large uncertainties in $\xi_{\mathrm{ion}}^{\mathrm{H\,II}}$ as we have significant scatter in our $\xi_{\mathrm{ion}}^{\mathrm{H\,II}}$ relative to T19; T19 measure $\sigma = 0.20$ while we measure a standard deviation of $\sigma = 0.35$, an ∼43% increase. This is not surprising as $\xi_{\mathrm{ion}}^{\mathrm{H\,II}}$ is dependent on the ionizing photon production and underlining UV continuum. High-z SFHs, for example, are diverse in duration and intensity (T. J. Looser et al. 2025, 2024), from which heterogeneity in metal enrichment from Type I and Type II supernovae leading to changes in the ionization output of high-mass stars is expected. In addition, variations in the slope of the IMF and nebular continuum contribution can significantly affect the UV at 1500 Å, further increasing the observed scatter. Different dust conditions, such as dust exposure to harder radiation fronts absent from standard dust laws, thus leading to an underestimation of the UV luminosity when employing Balmer decrements (V. Markov et al. 2023; R. L. Sanders et al. 2024), could also play a role, among variations in electron density, nonstellar ionizing sources, or more exotic stellar populations (for a deeper discussion see H. Katz et al. 2024). Nonetheless, we largely agree with the Hα–$\xi_{\rm ion}^{\rm H\,II}$ relation from T19, albeit with greater variation.

In comparison, we find it challenging to describe the relation between [O III] and $\xi_{\rm ion}^{\rm H\,II}$ as a simple scaling law. The conflation of metallicity with ionization and age leads to a systematic underprediction of $\xi_{\rm ion}^{\rm H\,II}$ in extremely metal-poor ionizers. We perform an error-weighted linear function for the quantities Hβ + [O III] EW and $\xi_{\rm ion}^{\rm H\,II}$, finding that assuming a linear relationship results in a 0.5 dex underestimation, though the diversity of our Hα sample makes this relation within the errors of our Hα EW relation (Equation (5)). As we mention in Section 7.1 and demonstrate in Figure 6, however, these representative samples predominately overlap in Hα EW space, suggesting that similar SFHs and metallicity degeneracies can be alleviated with sSFR measurements. We, therefore, caution that linear [O III] EW–$\xi_{\rm ion}^{\rm H\,II}$ relations may not be applicable in the high-z Universe.

8. Summary

We investigate a population calling into question the ubiquity of young galaxies possessing high Hβ + [O III] EWs with JADES NIRSpec spectroscopy; we summarize our methods and findings as follows.

1. We determine how the distribution of the ionizing photon efficiency ($\xi_{\rm ion}^{\rm H\,II}$) scales with H$\alpha$, [O III] λ5007, and Hβ + [O III] λ5007 EWs for $z \gtrsim 2$ (Figure 3). We find dissimilar trends between $\xi_{\rm ion}^{\rm H\,II}$ and the different line EWs, suggesting a physically motivated difference in the EW distributions of our sample. When we divide our sample into low-, medium-, and high-Hβ + [O III] EW samples, we find 37% of our medium-EW sample has elevated Hα EWs similar to our high-EW sample. This finding implies that weakened observed Hβ + [O III] λ5007 EWs are driven by suppressed [O III] emission compared to Hβ, indicative of low gas-phase metallicities. The combination of our Hα EW and $\log \xi_{\rm ion}^{\rm H\,II}$ measurements $\gtrsim$25.5 Hz erg^{-1} also suggests these faint, extremely metal-poor galaxies are indeed experiencing intense and recent star formation episodes, aligning with the notion of stochastic star formation in the context of the larger population studies of R. Endsley et al. (2023, 2024).
2. We combine `BPASS` + `CLOUDY` models with ~31 [O III] λ4363 emitters and $\hat{R}$-derived metallicities, finding metallicities less than $12 + \log({\rm O/H}) \approx 7.70$ ($0.1Z_\odot$) significantly reduce Hβ + [O III] EWs without impacting $\xi_{\rm ion}^{\rm H\,II}$. This nonlinear effect is observed in a clear metallicity gradient to lower Hβ + [O III] EWs and higher $\xi_{\rm ion}^{\rm H\,II}$ (Figure 5). We further demonstrate these extremely metal-poor ionizers are common above $z \sim 2$, yet comparatively rare in pre-JWST $z \lesssim 2$ and $z \sim 7$ studies. It is above $12 + \log({\rm O/H}) \approx 7.7$ where oxygen has a weak dependence on metallicity yet high [O III] λ5007/Hβ ratios, and so intense [O III] emitters were more likely to be identified, but in return, they were likely to be more chemically enriched ($7.7 \lesssim 12 + \log({\rm O/H}) \lesssim 8.3$), especially as the dynamic range of [O III]'s metallicity sensitivity is reduced in the high-z Universe. Metallicity effects were diminished and the luminosity-weighted ages setting the Balmer and [O III] EW relations with $\xi_{\rm ion}^{\rm H\,II}$ were more apparent.
3. We demonstrate extremely metal-poor efficient SFGs are excluded under reasonable EELG Hβ + [O III] selections, e.g., EW(Hβ + [O III]) > 700 Å (Figure 7). A sole selection of Hβ + [O III] has a bias toward (1) enriched systems with similar extreme radiation fields and (2) more evolved star-forming systems as the effect of extremely low metallicities at fixed $\xi_{\rm ion}^{\rm H\,II}$ is nonlinear. However, these systems can be identified through their Hα EWs.
4. We find our sample generally follows the Hα EW and $\xi_{\rm ion}^{\rm H\,II}$ relation from T19, further suggesting that high-z systems should be identified based on their Hα emission, i.e., their respective location along the star formation main sequence (Figure 6). However, we find significant scatter in our data, likely reflecting different ionization, age, dust, and nebular conditions. We find there is added degeneracy in interpreting Hβ + [O III] EW as a tracer of ionization as the [O III] EW is greatly reduced below $12 + \log({\rm O/H}) \approx 7.70$ ($0.1Z_\odot$) leading to ~1 dex scatter above Hβ + [O III] ≈ 300 Å. We further demonstrate the ionization efficiencies of our metal-poor galaxies are underpredicted when using Hβ + [O III] scaling relations, and thus we argue against [O III] as a sole tracer of high-z efficient ionizing systems.

Acknowledgments

This material is based upon work supported by the National Science Foundation Graduate Research Fellowship under grant No. 2137424. M.V.M. is supported by the National Science Foundation via AAG grant 2205519, the Wisconsin Alumni Research Foundation via grant MSN251397, and NASA via STScI grant JWST-GO-4426. E.C.L. acknowledges the support of an STFC Webb Fellowship (ST/W001438/1). A.J.B. acknowledges funding from the "FirstGalaxies" Advanced Grant from the European Research Council (ERC) under the European Union's Horizon 2020 research and innovation program (grant Agreement No. 789056). S.T. acknowledges support from the Royal Society Research grant G125142. Y.Z. acknowledges support from the JWST/NIRCam contract to the University of Arizona NAS5-02015. J.W. gratefully acknowledges support from the Cosmic Dawn Center through the DAWN Fellowship. The Cosmic Dawn Center (DAWN) is funded by the Danish National Research Foundation under grant No. 140. S.C. acknowledges support by European Union's HE ERC Starting grant No. 101040227—WINGS. C.S. acknowledges support from the Science and Technology Facilities Council (STFC), by the ERC through Advanced grant 695671 "QUENCH" and by the UKRI Frontier Research grant RISEandFALL.

Appendix
Case B Departure Galaxies in Our Sample

It is fascinating that galaxies exhibiting Balmer ratios less than the intrinsic ratio of Case B at $T = 1.5 \times 10^4$ K parallel the systematic offset with [O III] EW, are routinely [O III] λ4363 emitters, and have elevated $\xi_{\rm ion}^{\rm H\,II}$ values at fixed EW. $\xi_{\rm ion}^{\rm H\,II}$ is, however, highly susceptible to dust given the use of UV and

Hα, and thus our consistently high $\log \xi_{\rm ion}^{\rm H\,II}$ measurements above ≈25.5 Hz $\rm erg^{-1}$ are possibly biased considering we intentionally did not correct for dust for Case B departures. However, if we examine the medium- and high-EW Case B departure galaxies with the criteria from Section 7.1, we find median Hα EWs of ≈787 Å and 713 Å and [O III] EWs of ≈852 Å and 306 Å, respectively. These findings parallel our main findings, aligning with the notion that most extremely metal-poor galaxies are efficient ionizers with large Hα EWs but disparate [O III] EWs. We argue that this subsample is not primarily comprised of biased outliers but instead aligned with emerging pictures of high-z Case B departure galaxies. For example, C. Scarlata et al. (2024) identified a local object with an Hα/Hβ ratio of 2.620 ± 0.078 using MMT spectroscopy. From their incredibly high-S/N spectrum (e.g., detection of He II and [Ar IV] lines), they derive an $\rm O^{++}$ temperature of 15,380 ± 850 K (using [O III] λ4363), an [O III]/[O II] ratio of 11.80 ± 0.74, and an EW(Hβ) = 165 ± 14 Å, indicating a hard ionization front and high sSFR. C. Scarlata et al. (2024), interestingly, find gas metallicities less than 10% solar are required to reproduce their Balmer and oxygen line ratios, equivalent to our [O III]-deficient systems. Likewise, using the JADES public release data, W. McClymont et al. (2025) found 52 (14) galaxies above $z > 2$ ($z > 5.3$) with Balmer decrements more than 1σ below Case B up to $T = 2.0 \times 10^4$ K. W. McClymont et al. (2025) found these sub–Case B galaxies tend to have higher [O III]/[O II] ratios (>10), steeper UV slopes, Lyα emission, and low metallicities ($12 + \log(\rm O/H) < 7.7$), aligning again with our extremely metal-poor efficient ionizers.

However, the physical picture proposed by the above works differs. C. Scarlata et al. (2024) proposed lower Hα/Hβ ratios arise from a preferential scattering of Hα photons out of the line of sight, requiring asymmetric geometries and gas densities large enough for Balmer self-absorption and pumping to the $n = 2$ state. The resultant Balmer ratios then originate from the respective optical depths of the Balmer lines. In contrast, W. McClymont et al. (2025) explored Case C recombination (G. J. Ferland 1999) combined with density-bounded nebulae. In this case, lower Hα/Hβ ratios arise from continuum photons exciting the Lyman lines differently depending on the Lyman optical depth of the H II region, which then modifies the resultant cascade to the Balmer series. A main limitation identified by C. Scarlata et al. (2024) was the resultant recombination emission luminosity diminishing due to density-bounded nebulae, so W. McClymont et al. (2025) included gas turbulence indicative of the high-z Universe to maintain Balmer luminosity.

However, H. Yanagisawa et al. (2024) demonstrated that both proposed scenarios require specific construction. For example, for the case where Lyman lines are optically thin, there is the formation of density-bounded nebulae from rapid quenching events (<25 Myr) where high-density gas is briefly removed, as well as the "fine-tuning" of the Lyman optical depths; while for the case where Balmer lines are optically thick, there needs to be gas densities high enough to populate the $n = 2$ level of hydrogen as well as specific line of sites and gas geometry. We cannot comment much from our current analysis about the physical picture governing anomalous Balmer emitters (ABEs; W. McClymont et al. 2025), but we see they are typically efficient ionizers. Considering the suggested density-bounded model forms from miniquenched episodes, our high ionization efficiencies indicate extreme star formation is still present. The galaxies that removed their high-density gas may be back in a relative upturn of star formation, but we would then expect gas densities to approach Case B conditions unless large gas inhomogeneities are present. The proposed configuration of large hydrogen densities with specific geometries and lines of site removes Hα photons to decrease the Hα/Hβ ratio, meaning our Hα-derived ionization efficiencies are lower limits. However, as mentioned in Section 7.1, we are near the theoretical maximum for ionization efficiency, meaning there cannot be many more ionizing photons gained back. This scenario would be fine if dust was present to decrease ionization efficiency, but ABEs have the peculiar trend of elevated Hγ/Hβ ratios—the opposite direction of dust effects. A more detailed analysis and discussion are most certainly necessary but outside our current scope. Regardless, in addition to Lyα emission and high [O III] λ5007/[O II] $\lambda\lambda$3727, 3729 ratios, we demonstrate ABEs possess high ionization efficiencies, have high Hα EWs, and likely have extremely low metallicities ($12 + \log(\rm O/H) < 7.7$; $0.1 Z_\odot$) diminishing Hβ + [O III] EWs and their inclusion in EELG samples.

ORCID iDs

Isaac H. Laseter https://orcid.org/0000-0003-4323-0597
Michael V. Maseda https://orcid.org/0000-0003-0695-4414
Charlotte Simmonds https://orcid.org/0000-0003-4770-7516
Ryan Endsley https://orcid.org/0000-0003-4564-2771
Andrew J. Bunker https://orcid.org/0000-0002-8651-9879
Rachana Bhatawdekar https://orcid.org/0000-0003-0883-2226
Kristan Boyett https://orcid.org/0000-0003-4109-304X
Alex J. Cameron https://orcid.org/0000-0002-0450-7306
Stefano Carniani https://orcid.org/0000-0002-6719-380X
Mirko Curti https://orcid.org/0000-0002-2678-2560
Zhiyuan Ji https://orcid.org/0000-0001-7673-2257
Pierluigi Rinaldi https://orcid.org/0000-0002-5104-8245
Aayush Saxena https://orcid.org/0000-0001-5333-9970
Sandro Tacchella https://orcid.org/0000-0002-8224-4505
Chris Willott https://orcid.org/0000-0002-4201-7367
Joris Witstok https://orcid.org/0000-0002-7595-121X
Yongda Zhu https://orcid.org/0000-0003-3307-7525

References

Alberts, S., Lyu, J., Shivaei, I., et al. 2024, ApJ, 976, 224
Amorín, R. O., Pérez-Montero, E., Vílchez, J. M., et al. 2010, ApJL, 715, L128
Atek, H., Labbé, I., Furtak, L. J., et al. 2024, Natur, 626, 975
Becker, G. D., Bolton, J. S., Madau, P., et al. 2015, MNRAS, 447, 3402
Begley, R., McLure, R. J., Cullen, F., et al. 2025, MNRAS, 537, 3245
Blanc, G. A., Kewley, L., Vogt, F. P. A., & Dopita, M. A. 2015, ApJ, 798, 99
Bonaventura, N., Jakobsen, P., Ferruit, P., Arribas, S., & Giardino, G. 2023, A&A, 672, A40
Bosman, S. E. I., Davies, F. B., Becker, G. D., et al. 2022, MNRAS, 514, 55
Bouwens, R. J., Illingworth, G. D., Franx, M., et al. 2009, ApJ, 705, 936
Bouwens, R. J., Illingworth, G. D., Oesch, P. A., et al. 2010, ApJL, 708, L69
Bouwens, R. J., Illingworth, G. D., Oesch, P. A., et al. 2015, ApJ, 803, 34
Boyett, K., Bunker, A. J., Curtis-Lake, E., et al. 2024, MNRAS, 535, 1796
Boyett, K., Mascia, S., Pentericci, L., et al. 2022, ApJL, 940, L52
Bunker, A. J., Cameron, A. J., Curtis-Lake, E., et al. 2024, A&A, 690, A288
Bunker, A. J., Saxena, A., Cameron, A. J., et al. 2023, A&A, 677, A88
Calzetti, D., Armus, L., Bohlin, R. C., et al. 2000, ApJ, 533, 682
Cameron, A. J., Katz, H., Rey, M. P., & Saxena, A. 2023a, MNRAS, 523, 3516
Cameron, A. J., Katz, H., Witten, C., et al. 2024, MNRAS, 534, 523
Cameron, A. J., Saxena, A., Bunker, A. J., et al. 2023b, A&A, 677, A115
Cappellari, M. 2017, MNRAS, 466, 798
Cappellari, M. 2023, MNRAS, 526, 3273
Cardamone, C., Schawinski, K., Sarzi, M., et al. 2009, MNRAS, 399, 1191
Castellano, M., Belfiori, D., Pentericci, L., et al. 2023, A&A, 675, A121

Chevallard, J., & Charlot, S. 2016, MNRAS, 462, 1415
Chevallard, J., Charlot, S., Senchyna, P., et al. 2018, MNRAS, 479, 3264
Choi, J., Dotter, A., Conroy, C., et al. 2016, ApJ, 823, 102
Chon, S., Hosokawa, T., Omukai, K., & Schneider, R. 2024, MNRAS, 530, 2453
Choustikov, N., Katz, H., Saxena, A., et al. 2024, MNRAS, 529, 3751
Conroy, C., Villaume, A., van Dokkum, P. G., & Lind, K. 2018, ApJ, 854, 139
Cueto, E. R., Hutter, A., Dayal, P., et al. 2024, A&A, 686, A138
Cullen, F., Carnall, A. C., Scholte, D., et al. 2025, MNRAS, 540, 2176
Curti, M., D'Eugenio, F., Carniani, S., et al. 2023a, MNRAS, 518, 425
Curti, M., Maiolino, R., Carniani, S., et al. 2024, A&A, 684, A75
Davé, R., Oppenheimer, B. D., & Finlator, K. 2011, MNRAS, 415, 11
Davis, K., Trump, J. R., Simons, R. C., et al. 2024, ApJ, 974, 42
D'Eugenio, F., Cameron, A. J., Scholtz, J., et al. 2025, ApJS, 277, 4
Donnan, C. T., McLeod, D. J., Dunlop, J. S., et al. 2023, MNRAS, 518, 6011
Dors, O. L. 2021, MNRAS, 507, 466
Dreizler, S., & Werner, K. 1993, A&A, 278, 199
Duncan, K., & Conselice, C. J. 2015, MNRAS, 451, 2030
Eisenstein, D. J., Johnson, B. D., Robertson, B., et al. 2023, arXiv:2310.12340
Eldridge, J. J., & Stanway, E. R. 2009, MNRAS, 400, 1019
Emami, N., Siana, B., Alavi, A., et al. 2020, ApJ, 895, 116
Endsley, R., Stark, D. P., Whitler, L., et al. 2023, MNRAS, 524, 2312
Endsley, R., Stark, D. P., Whitler, L., et al. 2024, MNRAS, 533, 1111
Eyles, L. P., Bunker, A. J., Ellis, R. S., et al. 2007, MNRAS, 374, 910
Eyles, L. P., Bunker, A. J., Stanway, E. R., et al. 2005, MNRAS, 364, 443
Ferland, G. J. 1999, PASP, 111, 1524
Ferland, G. J., Chatzikos, M., Guzmán, F., et al. 2017, RMxAA, 53, 385
Ferruit, P., Jakobsen, P., Giardino, G., et al. 2022, A&A, 661, A81
Finkelstein, S. L., Ryan Russell, E. J., Papovich, C., et al. 2015, ApJ, 810, 71
Giavalisco, M., Ferguson, H. C., Koekemoer, A. M., et al. 2004, ApJL, 600, L93
González, V., Labbé, I., Bouwens, R. J., et al. 2010, ApJ, 713, 115
Gräfener, G., Koesterke, L., & Hamann, W. R. 2002, A&A, 387, 244
Groves, B., Brinchmann, J., & Walcher, C. J. 2012, MNRAS, 419, 1402
Guo, Z., Zhang, Z.-Y., Yan, Z., et al. 2024, ApJ, 970, 136
Gutkin, J., Charlot, S., & Bruzual, G. 2016, MNRAS, 462, 1757
Hashimoto, T., Garel, T., Guiderdoni, B., et al. 2017, A&A, 608, A10
Heintz, K. E., Brammer, G. B., Giménez-Arteaga, C., et al. 2023, NatAs, 7, 1517
Heintz, K. E., Brammer, G. B., Watson, D., et al. 2025, A&A, 693, A60
Henry, A., Scarlata, C., Martin, C. L., & Erb, D. 2015, ApJ, 809, 19
Hopkins, P. F., Richards, G. T., & Hernquist, L. 2007, ApJ, 654, 731
Hutter, A., Cueto, E. R., Dayal, P., et al. 2025, A&A, 694, A254
Inayoshi, K., Harikane, Y., Inoue, A. K., Li, W., & Ho, L. C. 2022, ApJL, 938, L10
Jaskot, A. E., & Oey, M. S. 2013, ApJ, 766, 91
Katz, H., Cameron, A. J., Saxena, A., et al. 2024, arXiv, arXiv:2408.03189
Katz, H., Saxena, A., Cameron, A. J., et al. 2023, MNRAS, 518, 592
Kewley, L. J., Dopita, M. A., Leitherer, C., et al. 2013, ApJ, 774, 100
Kobayashi, C., & Ferrara, A. 2024, ApJL, 962, L6
Kong, X., Cheng, F. Z., Weiss, A., & Charlot, S. 2002, A&A, 396, 503
Labbé, I., González, V., Bouwens, R. J., et al. 2010, ApJL, 716, L103
Labbé, I., Oesch, P. A., Bouwens, R. J., et al. 2013, ApJL, 777, L19
Lam, D., Bouwens, R. J., Labbé, I., et al. 2019, A&A, 627, A164
Lambrides, E., Garofali, K., Larson, R., et al. 2024, arXiv, arXiv:2409.13047
Laseter, I. H., Maseda, M. V., Curti, M., et al. 2024, A&A, 681, A70
Looser, T. J., D'Eugenio, F., Maiolino, R., et al. 2025, A&A, 697, A88
Looser, T. J., D'Eugenio, F., Maiolino, R., et al. 2024, Natur, 629, 53
Lyu, J., Alberts, S., Rieke, G. H., et al. 2024, ApJ, 966, 229
Maiolino, R., & Mannucci, F. 2019, A&ARv, 27, 3
Maiolino, R., Scholtz, J., Curtis-Lake, E., et al. 2024, A&A, 691, A145
Maiolino, R., Scholtz, J., Witstok, J., et al. 2024, Natur, 627, 59
Markov, V., Gallerani, S., Pallottini, A., et al. 2023, A&A, 679, A12
Mármol-Queraltó, E., McLure, R. J., Cullen, F., et al. 2016, MNRAS, 460, 3587
Mascia, S., Pentericci, L., Calabrò, A., et al. 2024, A&A, 685, A3
Maseda, M. V., Bacon, R., Franx, M., et al. 2018, ApJL, 865, L1
Maseda, M. V., Bacon, R., Lam, D., et al. 2020, MNRAS, 493, 5120
Maseda, M. V., Lewis, Z., Matthee, J., et al. 2023, ApJ, 956, 11
Maseda, M. V., van der Wel, A., Rix, H.-W., et al. 2014, ApJ, 791, 17
Massey, P., Bresolin, F., Kudritzki, R. P., Puls, J., & Pauldrach, A. W. A. 2004, ApJ, 608, 1001
McClymont, W., Tacchella, S., D'Eugenio, F., et al. 2025, MNRAS, 540, 190
Mitra, S., Ferrara, A., & Choudhury, T. R. 2013, MNRAS, 428, L1
Murphy, E. J., Condon, J. J., Schinnerer, E., et al. 2011, ApJ, 737, 67
Nagamine, K., Ouchi, M., Springel, V., & Hernquist, L. 2010, PASJ, 62, 1455
Nakajima, K., Ellis, R. S., Iwata, I., et al. 2016, ApJL, 831, L9
Nakajima, K., Ouchi, M., Isobe, Y., et al. 2023, ApJS, 296, 33
Oke, J. B., & Gunn, J. E. 1983, ApJ, 266, 713
Ono, Y., Ouchi, M., Shimasaku, K., et al. 2010, ApJ, 724, 1524
Osterbrock, D. E., & Ferland, G. J. 2006, Astrophysics of Gaseous Nebulae and Active Galactic Nuclei (Mill Valley, CA: Univ. Science Books)
Paardekooper, J.-P., Khochfar, S., Dalla Vecchia, C., et al. 2015, MNRAS, 451, 2544
Pacucci, F., & Narayan, R. 2024, ApJ, 976, 96
Pallottini, A., & Ferrara, A. 2023, A&A, 677, L4
Planck Collaboration, Aghanim, N., Akrami, Y., et al. 2020, A&A, 641, A6
Prieto-Lyon, G., Strait, V., Mason, C. A., et al. 2023, A&A, 672, A186
Reddy, N. A., Oesch, P. A., Bouwens, R. J., et al. 2018a, ApJ, 853, 56
Reddy, N. A., Shapley, A. E., Sanders, R. L., et al. 2018b, ApJ, 869, 92
Reddy, N. A., Topping, M. W., Sanders, R. L., Shapley, A. E., & Brammer, G. 2023, ApJ, 952, 167
Rhoads, J. E., Wold, I. G. B., Harish, S., et al. 2023, ApJL, 942, L14
Rieke, M. J., Robertson, B., Tacchella, S., et al. 2023, ApJS, 269, 16
Rinaldi, P., Caputi, K. I., Costantin, L., et al. 2023, ApJ, 952, 143
Rinaldi, P., Caputi, K. I., Iani, E., et al. 2024, ApJ, 969, 12
Roberts-Borsani, G., Treu, T., Shapley, A., et al. 2024, ApJ, 976, 193
Robertson, B. E., Furlanetto, S. R., Schneider, E., et al. 2013, ApJ, 768, 71
Sanders, R. L., Shapley, A. E., Kriek, M., et al. 2018, ApJ, 858, 99
Sanders, R. L., Shapley, A. E., Topping, M. W., Reddy, N. A., & Brammer, G. B. 2023a, ApJ, 955, 54
Sanders, R. L., Shapley, A. E., Topping, M. W., Reddy, N. A., & Brammer, G. B. 2023b, arXiv:2303.08149
Sanders, R. L., Shapley, A. E., Topping, M. W., et al. 2024, arXiv, arXiv:2408.05273
Sandles, L., D'Eugenio, F., Maiolino, R., et al. 2024, A&A, 691, A305
Sarkar, A., Chakraborty, P., Vogelsberger, M., et al. 2025, ApJ, 978, 136
Saxena, A., Bunker, A. J., Jones, G. C., et al. 2024a, A&A, 684, A84
Saxena, A., Cameron, A. J., Katz, H., et al. 2024b, arXiv, arXiv:2411.14532
Scarlata, C., Hayes, M., Panagia, N., et al. 2024, arXiv, arXiv:2404.09015
Schaerer, D., & de Barros, S. 2009, A&A, 502, 423
Schaerer, D., & de Barros, S. 2010, A&A, 515, A73
Scholte, D., Cullen, F., Carnall, A. C., et al. 2025, MNRAS, 540, 1800
Scholtz, J., Maiolino, R., D'Eugenio, F., et al. 2025, A&A, 697, A175
Shen, L., Papovich, C., Matharu, J., et al. 2025, ApJ, 980, 45
Shen, X., Hopkins, P. F., Faucher-Giguère, C.-A., et al. 2020, MNRAS, 495, 3252
Simmonds, C., Tacchella, S., Maseda, M., et al. 2023, MNRAS, 523, 5468
Simmonds, C., Tacchella, S., Hainline, K., et al. 2024, MNRAS, 535, 2998
Smit, R., Bouwens, R. J., Labbé, I., et al. 2014, ApJ, 784, 58
Stanway, E. R., McMahon, R. G., & Bunker, A. J. 2005, MNRAS, 359, 1184
Stark, D. P., Auger, M., Belokurov, V., et al. 2013, MNRAS, 436, 1040
Stark, D. P., Ellis, R. S., Charlot, S., et al. 2017, MNRAS, 464, 469
Stark, D. P., Walth, G., Charlot, S., et al. 2015, MNRAS, 454, 1393
Steidel, C. C., Strom, A. L., Pettini, M., et al. 2016, ApJ, 826, 159
Sun, G., Faucher-Giguère, C.-A., Hayward, C. C., & Shen, X. 2023a, MNRAS, 526, 2665
Sun, G., Faucher-Giguère, C.-A., Hayward, C. C., et al. 2023b, ApJ, 955, 35
Tacchella, S., Smith, A., Kannan, R., et al. 2022, MNRAS, 513, 2904
Tang, M., Stark, D. P., Chevallard, J., & Charlot, S. 2019, MNRAS, 489, 2572
Taylor, A. J., Barger, A. J., & Cowie, L. L. 2022, ApJL, 939, L3
Topping, M. W., Stark, D. P., Endsley, R., et al. 2024a, MNRAS, 529, 4087
Topping, M. W., Stark, D. P., Senchyna, P., et al. 2024b, MNRAS, 529, 3301
Trump, J. R., Haro, P. A., Simons, R. C., et al. 2023, ApJ, 945, 35
Van der Wel, A., Straughn, A. N., Rix, H. W., et al. 2011, ApJ, 742, 111
Weinmann, S. M., Neistein, E., & Dekel, A. 2011, MNRAS, 417, 2737
Welch, B. L. 1947, Biometrika, 34, 28
Whitler, L., Stark, D. P., Topping, M. W., et al. 2025, arXiv, arXiv:2501.00984
Wilkins, S. M., Bunker, A. J., Stanway, E., Lorenzoni, S., & Caruana, J. 2011, MNRAS, 417, 717
Wilkins, S. M., Lovell, C. C., Fairhurst, C., et al. 2020, MNRAS, 493, 6079
Willott, C. J., Delorme, P., Reylé, C., et al. 2010, AJ, 139, 906
Xiao, L., Stanway, E. R., & Eldridge, J. J. 2018, MNRAS, 477, 904
Yanagisawa, H., Ouchi, M., Nakajima, K., et al. 2024, ApJ, 974, 180
Yung, L. Y. A., Somerville, R. S., Finkelstein, S. L., Wilkins, S. M., & Gardner, J. P. 2024, MNRAS, 527, 5929
Zheng, Z., Cen, R., Trac, H., & Miralda-Escudé, J. 2010, ApJ, 716, 574
Zhu, Y., Alberts, S., Lyu, J., et al. 2025, ApJ, 986, 18